Protoliths and metamorphism of the central Himalayan eclogites: Zircon/titanite U–Pb geochronology, Hf isotope and geochemistry

Xin Dong[a, *], Zeming Zhang[a], Zuolin Tian[a], Yaoling Niu[b], Liangliang Zhang[c]

[a] Key Laboratory of Deep-Earth Dynamics of Ministry of Natural Resources, Institute of Geology, Chinese Academy of Geological Sciences, Beijing, 100037, China

[b] Department of Earth Sciences, Durham University, Durham DH1 3LE, UK

[c] State Key Laboratory of Geological Processes and Mineral Resources, and Institute of Earth Sciences, China University of Geosciences, Beijing 100083, China

ABSTRACT

The retrograded high-pressure (HP) eclogites in the central Himalaya provide insights into the metamorphic history of the deep crust beneath the Tibetan plateau. Due to the paucity of exposure, the nature and timing of the protolith and metamorphism of the eclogites remain poorly known. Here we report zircon and titanite U–Pb ages, bulk-rock and mineral compositions and zircon Hf isotope data on the eclogites from the Thongmön and Kharta areas in the central Himalaya. The eclogites record peak HP eclogite-facies metamorphism at >1.6 GPa, high-temperature to ultrahigh-temperature (HT-UHT) granulite-facies overprinting (ca. 0.88–0.99 GPa and 875–920 °C), and subsequent decompression-cooling retrograde metamorphism (ca. 0.42–0.62 GPa and 800–820 °C). Geochemical data suggest that the eclogite protoliths are most consistent with being seafloor tholeiitic basalts with an E-MORB signature. Inherited magmatic zircon cores from the eclogites give a protolith age of ~ 450 Ma and $\varepsilon_{Hf}(t)$ values of + 3.2 to + 7.0. The mantle portions of the zircons record a metamorphic overgrowth, and the rims reflect zircon growth associated with an early decompression granulite-facies metamorphism (~ 17.9–15.3 Ma) and later decompression-cooling retrograde metamorphic (~ 14.8–13.3 Ma). The titanite U–Pb age (~ 15.4 Ma) further indicates the beginning of the later retrograde metamorphism. All these data and observations allow the proposal that in contrast to the ultrahigh-pressure (UHP) eclogites in the western Himalayan syntaxis, the HP eclogites in the central Himalaya record the long-lived burial of the Indian continental crust since initial Indo-Asia collision at ~ 55 Ma.

Keywords: Zircon and titanite U–Pb dating, Geochemistry, Protolith and metamorphic ages, HP eclogite, Central Himalaya

1. Introduction

The Himalayan orogeny is a tectonic response to the continued India-Asia convergence since the initial continental collision at ~ 55 Ma (e.g., Yin and Harrison, 2000; Najman et al., 2010). As the orogenic core, the Greater Himalayan Sequences (GHS) record critical information for understanding this classic orogenesis. Eclogites, as one of the important metabasic rock components of the GHS, are expected to record the history of the underthrusting Indian crust beneath the Asian plate, and to contain important information on the nature, timing and duration of the metamorphism and the burial–exhumation of crustal material from beneath the Tibetan plateau (e.g., Cottle et al., 2009a). Two types of eclogites in the GHS have been reported (e.g., Lombardo and Rolfo, 2000). The UHP coesite-bearing eclogites have been documented to be metamorphosed up to >2.6 GPa during the initial India-Asia collision, cropping out within or close to the Indus-Tsangpo suture zone (ITSZ, i.e., the India-Asia suture zone) in the western Himalaya (e.g., Tso Morari in Ladakh and Kaghan in NW Pakistan) (Guillot et al., 2008 and references therein). In contrast, the HP eclogites have been reported in the central Himalaya, including the Ama Drime Massif (ADM) and its adjacent areas of China (e.g., Lombardo et al., 1998; Groppo et al., 2007; Liu et al., 2007; Cottle et al., 2009b; Kellett et al., 2014; Wang et al., 2017a, 2021; Li et al., 2019), Laya of northwestern Bhutan (e.g., Chakungal et al., 2010; Grujic et al., 2011; Warren et al., 2011), Sikkim in India (Rolfo et al., 2008) and Arun Valley in Nepal (Corrie et al., 2010), all of which are hundreds of kilometers south of the ITSZ (Fig. 1).

These HP eclogites in the central Himalaya show textures compatible with initial eclogite-facies equilibration, followed by pervasive and strong overprints of later granulite-facie metamorphism (i.e., granulitized eclogite; e.g., Lombardo and Rolfo, 2000; Groppo et al., 2007; Rolfo et al., 2008; Cottle et al., 2009b; Chakungal et al., 2010; Warren et al., 2011, Wang et al., 2017a, 2021; Li et al., 2019). Three distinct peak metamorphic ages have been proposed, including (1) Eocene (ca. 38 Ma, Kellett et al., 2014); (2) late Oligocene (ca. 26–23 Ma, Corrie et al., 2010) and (3) Miocene (ca. 17–14 Ma, Grujic et al., 2011; Wang et al., 2017a; Li et al., 2019). However, the interpretation of Miocene ages is still controversial, representing eclogite-facies ages or granulite-facie ages (e.g., Li et al., 2019; Wang et al., 2021). Moreover, the protoliths of the HP eclogites have been interpreted as the Proterozoic and Paleozoic continental basalts (Chakungal et al., 2010; Wang et al., 2017a) or the Miocene mantle-derived mafic dikes (Grujic et al., 2011). Therefore, the timing of the metamorphism and the protoliths of the HP eclogites are both unconstrained.

For the above reasons, we have carried out a comprehensive study on the HP eclogites sampled from the GHS in the Thongmön and Kharta areas in the central Himalaya using bulk-rock elemental compositions, mineral chemistry, zircon and titanite geochronology and zircon Hf isotopic data. We come to the conclusions that the protoliths of the HP eclogites are seafloor tholeiitic basalts of Ordovician age, and the granulite-facie metamorphism can be constrained to occur in the Miocene (~ 17.9–13.3 Ma).

2. Geological setting and samples

The Himalayan orogenic belt, spanning ~ 2500 km, has been subdivided, from north to south, into three lithotectonic units—the Tethyan, Greater and Lesser Himalayan Sequences (THS, GHS and LHS, respectively) separated by the South Tibetan Detachment System (STDS) and the Main Central Thrust (MCT) (e.g., Yin, 2006; Kohn, 2014). The THS separated by the STDS from the GHC and the ITSZ to the north is mainly composed of the Late Proterozoic to Mesozoic metasedimentary sequence metamorphosed under lower amphibolite-facies conditions or unmetamorphosed (cf. Kohn, 2014 and references therein). As the orogenic core, the GHS, representing the middle to lower crustal material, is composed of high-grade metamorphic rocks (typically upper-amphibolite to granulite facies) with protoliths of the Late Proterozoic to Paleozoic sedimentary and magmatic rocks (e.g., Searle et al. 2003; Goscombe et al. 2006; Cawood et al. 2007; Kohn 2008; Groppo et al. 2009; Imayama et al. 2010; Wang et al. 2013, 2015). The STDS is a system of one to several low-angle normal brittle faults and/or ductile shears dipping to the north (e.g., Burchfiel et al. 1992; Cottle et al. 2007; Leloup et al. 2010; Grujic et al., 2011). The Main Central Thrust Zone (MCTZ) is a top-to-the-south thrust ductile shear zone and separates the hanging-wall GHS rocks from the footwall greenschist-facies to amphibolite-facies LHS rocks (e.g., Searle et al. 2008; Grujic et al., 2011).

The HP eclogites of this study were collected in the Thongmön and Kharta areas of the central Himalaya (Figs. 1 and 2). The lithotectonic units in the region include the THS and GHS (e.g., Groppo et al. 2007; Jessup et al. 2008; Kali et al. 2010). The GHS in the studied areas consists of metabasic rocks, gneisses and schists, all of which are locally crosscut by leucogranite (Liu et al., 2007; Cottle et al., 2009b; Li et al., 2019). The HP eclogites and their granulitized equivalents occur within paragneiss and schists as lenses or elongate blocks, ranging from several tens of centimeters to tens of meters in length (Fig. 3). Sample details, including locations, mineral assemblages, protolith and metamorphic ages, and zircon $\varepsilon_{Hf}(t)$ data are given in Table

1.

3. Petrography

The HP eclogites (granulitized eclogites) display a porphyroblastic texture and contain garnet, clinopyroxene, orthopyroxene, plagioclase, amphibole, quartz and biotite with accessory apatite, zircon, rutile, ilmenite, titanite and magnetite. The coarse-grained garnets occur as porphyroblasts and mostly have a mineral inclusion-rich core and a nearly inclusion-free rim (Fig. 4a and g).

The granulitized eclogites preserve primary omphacite and rutile inclusions in garnet cores (Fig. 4a–c) and textural evidence for earlier eclogite-facies metamorphism, i.e., a distinctive lacy symplectite of clinopyroxene + Na-rich plagioclase developed as a result of omphacite decompression/decomposition (Fig. 4d–f). However, some omphacite inclusions in garnet core are also replaced by clinopyroxene + Na-rich plagioclase (Fig. 4g–i). High-temperature granulite-facies event is represented by the development of a Ca-rich plagioclase + orthopyroxene ± amphibole or Ca-rich plagioclase + amphibole symplectite around garnet (Fig. 4a and j). In a late medium-pressure (MP) granulite-facies stage, amphiboles have grown after clinopyroxene-plagioclase or orthopyroxene-plagioclase symplectites and normally include relics of these symplectites and inclusions of ilmenite and magnetite (Fig. 4a, d–f). Within symplectite of clinopyroxene + Na-rich plagioclase, minor titanite rims ilmenite (Fig. 4k–m). Rare biotite grows with plagioclase together in the matrix.

At least three mineral assemblages have been identified to reflect three events as described above, i.e., eclogite-facies (M1) of Grt core + Omp + Rt + Ilm, HT granulite-facies (M2) of Grt rim + Cpx + Opx + Amp + Ca-rich Pl + Ilm, and MP granulite-facies (M3) of Amp + Pl + Bt + Cpx + Opx + Ilm+ Mt.

4. Analytical methods

Cathodoluminescence (CL) and back-scattered-electron (BSE) images obtained by a TESCAN Integrated Mineral Analyzer (TIMA) at the Institute of Geology, Chinese Academy of Geological Sciences (CAGS), Beijing, were used to characterize sample textures and to select zircon/titanite spots for U–Pb dating and zircon Hf isotope analysis. An automated mineralogy approach has been adopted for phase/mineral and element distribution mapping obtained by TIMA. The analyses were performed on the thin section with a 25 kV accelerating voltage, 7.55 nA beam current, 15 mm working distance and 91.67 nm spot size.

Mineral compositions were analyzed in the Institute of Geology, CAGS, Beijing, using a JEOL JXA 8900 electron probe microanalyzer (EPM) with 15 kV accelerating voltage, 20 nA beam current, 10 μm probe diameter, and counting time of 10 s for peak and background. Natural or synthetic standards were used for calibrating EPM analysis with ZAF corrections applied.

Bulk-rock major and trace element analysis was done at the National Geological Analysis Center of China, CAGS, Beijing. The major element analysis was done using X-ray fluorescence (XRF, Rigaku-3080). The trace elements Zr, Nb, Cr, Sr, Ba, Ni, Rb and Y were analyzed using a different XRF instrument (Rigaku-2100). Other trace elements were analyzed by using inductively coupled plasma mass spectrometry (ICP-MS, TJA-PQ-ExCell) following Li (1997).

Zircon U–Pb dating and trace element analysis were done using LA-ICPMS in the Mineral and Fluid inclusion microanalysis Laboratory, CAGS. An NWR 193^{UC} laser ablation system (Elemental Scientific Lasers, USA) was equipped with Coherent Excistar 200 excimer laser and a Two Volume 2 ablation cell. The laser ablation system was coupled to an Agilent 7900 ICPMS (Agilent, USA). The analytical details are given in Yu et al. (2019). The analysis was done using 25 μm diameter spot at 5 Hz and a fluence of 2 J/cm^2. Iolite software package was used to calibrate the downhole fractionation and data reduction (Paton et al., 2010). Zircon 91500 and GJ-1 were used as primary and secondary reference materials, respectively. NIST610 and ^{91}Zr were used to calibrate the trace element concentrations as external reference material and internal standard, respectively. The measured ^{206}Pb/^{238}U weighted mean age of zircon 91500 in the batch is 1062.1 ± 1.7 Ma (MSWD = 0.55, 2σ, n = 61). Concordia diagrams and weighted mean calculations were made using Isoplot/Ex_ver3 (Ludwig, 2003). Data-point errors are ±1σ.

Zircon Hf isotope analysis was done using a GeoLas Pro UP193nm laser-ablation microprobe, attached to a Neptune multi-collector ICP-MS in the MNR Key Laboratory of Metallogeny and Mineral Assessment, Institute of Mineral Resources, CAGS, Beijing. Instrumental conditions and data acquisition were detailed in Hou et al. (2007). A stationary spot was used during the analysis, with a beam diameter of 44 μm at 8 Hz and a fluence of 8-10 J/cm^2. In order to correct for isobaric interferences of ^{176}Lu and ^{176}Yb on ^{176}Hf, $^{176}Lu/^{175}Lu = 0.02658$ and $^{176}Yb/^{173}Yb = 0.796218$ ratios were determined (Chu et al., 2002). For instrumental mass bias correction Yb isotope ratios were normalized to $^{172}Yb/^{173}Yb$ of 1.35274 and Hf isotope ratios to $^{179}Hf/^{177}Hf$ of 0.7325 using an exponential law (Chu et al., 2002). Zircon GJ1 was used as the reference standard, with a weighted mean $^{176}Hf/^{177}Hf$ ratio of 0.282018 ± 0.000020 (2σ, n = 3) during our routine analysis, which is essentially the same as the weighted mean $^{176}Hf/^{177}Hf$ ratio of 0.282013 ± 0.000019 (2σ) by Elhlou et al. (2006).

Titanite U–Pb dating were carried out using LA-ICP-MS in the Milma Lab. of China University of Geosciences (Beijing). Detailed analytical procedure is given in Sun et al. (2012). The beam diameter of the laser was set to 35 µm. The titanite standard BLR-1 was analyzed as an external standard. Another standard MKED1 was analyzed as unknowns to check the data accuracy, which yielded a mean $^{206}Pb/^{238}U$ age of 1518 ± 33 Ma (MSWD = 1.5, 1σ, n = 6). The results are identical within error to the recommended values (1517 ± 0.3 Ma, Spandler et al., 2016). The measured, uncorrected, compositions of titanite were plotted on a Tera–Wasserburg diagram (Tera and Wasserburg, 1972), and they define a line which intersects the y-axis at the common $^{207}Pb/^{206}Pb$ value. The measured ^{207}Pb was applied for common-Pb correction using the two-stage model of Stacey and Kramers (1975), and the $^{206}Pb/^{238}U$ weighted mean ages were calculated using Isoplot/Ex_ver3 (Ludwig, 2003). Data-point error symbols are ±1σ.

5. Results

5.1. Mineral major element data

Representative mineral compositions for garnet, pyroxene, plagioclase and amphibole in sample T15-5-7 are given in Supplementary Table 1–4, respectively.

Garnet is characterized by almandine (41–47 mol.%), grossular (23–32 mol.%), pyrope (23–29 mol.%) and minor spessartine (2 mol.%), retaining compositional zoning. The garnet cores (inclusion-rich) has higher Fe, Mg and Mn and lower Ca contents than the rims (inclusion-free) (Figs. 4c, h and 5a). The core compositions are essentially uniform, suggesting that they have been largely homogenized at high temperature (Fig. 5a, Florence and Spear, 1991; Spear, 1991; Kohn and Spear, 2000).

Clinopyroxene has been identified into three types, according to its microstructure as described above and compositions, including (1) omphacite occurs as inclusions in garnet; (2) clinopyroxene occurs as symplectite with Na-rich plagioclase after omphacite in the matrix, (3) clinopyroxene occurs as inclusions in garnet, retrogressive product of precursor omphacite or prograde relict. Omphacite has jadeite component contents ranging from 20 mol.% to 26 mol.% (Fig. 5b) and X_{Na} (Na/(Na+Ca)) values of 0.21–0.26. The clinopyroxene as symplectite in the matrix is augite (Fig. 5c), with low X_{Na} values of 0.046–0.056. The clinopyroxene as inclusions in garnet is also augite (Fig. 5c), with X_{Na} values of 0.034–0.234. Orthopyroxene is enstatite with the end-member components $En_{0.58–0.59}Fs_{0.39–0.40}Wo_{0.01–0.03}$ (Fig. 5c).

Plagioclase has been grouped into three types, based on its microstructure as described above. The first type of plagioclase forms fine-grained intergrowths of clinopyroxene as symplectite in the matrix, or occurs with clinopyroxene as inclusions in garnet, developed after omphacite decomposition with andesine ($An_{47–49}$) composition. The second type of plagioclase occurring with orthopyroxene as symplectite around garnet is labradorite, bytownite and anorthite ($An_{69–92}$). The third type of plagioclase occurring in the matrix is labradorite ($An_{51–53}$).

Amphibole has been identified into two types, according to its microstructure as described above. Although two types of amphibole are all pargasite, amphibole occurring as symplectite around garnet has higher Ti (0.190–0.217 a.p.f.u.) and Al (2.248–2.435 a.p.f.u.) than those occurring in the matrix (Ti = 0.134–0.135 a.p.f.u. and Al = 2.136–2.229 a.p.f.u.).

5.2. Bulk-rock major and trace element data

Bulk-rock major and trace element compositions of the HP eclogites are given in Supplementary Table 5. They have basaltic SiO_2 (42.7–51.6 wt.%), relatively higher FeOt (11.3–16.0 wt.%) and TiO_2 (1.26–2.85 wt.%) than calc-alkaline rocks, indicating a tholeiitic basalt protolith (Fig. 6a–c). They have a weak fractionated REE pattern ([La/Yb]n = 1.23–2.08, Fig. 7a), and show significant positive Rb, U and Pb anomalies (Fig. 7b), reflecting fluid related enrichment.

5.3. Zircon U–Pb age and Hf isotope

Zircon U–Pb age data of four samples and Hf isotopic compositions of two samples are given in Supplementary Tables 6 and 7, respectively.

Zircons from samples T15-15-5 and T15-10-1 are subhedral–euhedral oblong or prismatic with varying size (~ 50–200 μm). CL images show two types of zircons.

One type shows a core–rim structure consisting of inherited cores with oscillatory zoning and dark rims without zoning (Fig. 8a and b). The other type shows weak sector or fir-tree zoning (Fig. 8b). The analyzed spots on zircon cores yield weighted mean $^{206}Pb/^{238}U$ ages of 449 ± 2 Ma (n = 38, MSWD = 0.84) and 447 ± 3 Ma (n = 10, MSWD = 0.85) (Fig. 9a and c), and relatively high REE contents and fractionated patterns (Fig. 10a and c). The 43 Hf isotopic analyses on zircon cores give $\varepsilon_{Hf}(t) > 0$ (+ 3.2 to + 7.0; Fig. 11). Analyzed spots on zircon rims yield $^{206}Pb/^{238}U$ ages of 15.3 ± 0.9 Ma (n = 9, MSWD = 1.4) and 17.9 ± 0.2 Ma (n = 21, MSWD = 3.1) (Fig. 9b and d), and lower REE contents than the core domains and flat HREE patterns (Fig. 10b and d). Analyzed spots on the second type of zircons from sample T15-10-1 yield a mean $^{206}Pb/^{238}U$ age of 13.9 ± 0.1 Ma (n = 22, MSWD = 1.9) (Fig. 9d) with higher REE contents and steeper HREE patterns than zircon rims of the first zircon type (Fig. 10d).

Zircons from samples T15-17-2 and T15-7-3 are subhedral–euhedral prismatic or oblong with varying size (~ 100–200 μm). CL images show that most zircons have a core–mantle–rim structure. The cores are rich in inclusions, mostly overprinted by mantle; the mantles show patchy zoning with relatively bright luminescence (too narrow to analyze for T15-7-3); the rims show dark luminescence without zoning (some zircons from T15-17-2 are without rims, Fig. 8c). The analyzed spots on zircon mantles of sample T15-17-2 yield a mean $^{206}Pb/^{238}U$ age of 15.5 ± 0.1 Ma (n = 30, MSWD = 0.71) (Fig. 9e), with a relatively flat HREE pattern than zircon rims (Fig. 10e). Analyzed spots on zircon rims yield weighted mean $^{206}Pb/^{238}U$ ages of 13.3 ±

0.2 Ma (n = 5, MSWD = 2.2) and 14.8 ± 0.1 Ma (n = 33, MSWD = 1.9) (Fig. 9e and f), with a steep HREE pattern (Fig. 10e and f).

5.4. Titanite U–Pb age

One titanite-rich sample T15-10-1 was selected for LA-ICP-MS titanite U–Pb dating. SE and BSE images of representative titanite are shown in Supplementary Fig. 1 and the titanite U–Pb age data are given in Supplementary Table 8.

Titanites are subhedral–anhedral with varying size (~ 50–200 μm) without zoning. The analyzed spots yield lower intercept age of 15.3 ± 0.3 Ma (Fig. 12a). After correction using ^{207}Pb, the $^{206}Pb/^{238}U$ weighted mean age is 15.4 ± 0.2 Ma (n = 39, MSWD = 1.2) (Fig. 12b).

6. Metamorphic *P-T* conditions

6.1. Phase equilibria modelling

The metamorphic conditions of sample T15-5-7 were estimated using *P–T* pseudosection modeling. The pseudosection and mineral composition isopleths were done using computer program GeoPS (ver. 2.9, Xiang et al., 2020) and the thermodynamic data set of Holland and Powell (2011, hp62ver.dat) for the multi-component system Na_2O – CaO - K_2O – FeO – MgO - Al_2O_3 - SiO_2 - H_2O - TiO_2 - O_2 (NCKFMASHTO). The pseudosection has been calculated using the following activity-solution models: biotite, garnet and orthopyroxene (White et al., 2014); K-feldspar and plagioclase (Holland and Powell, 2003); ilmenite (White et al., 2000); amphibole, augite and melt (Green et al., 2016); muscovite (Coggon and Holland, 2002; Auzanneau et al., 2010); omphacite (Green et al., 2007); epidote and clinozoisite (Holland and Powell, 1998). Quartz, rutile, H_2O and titanite were regarded as pure endmember phases. Omphacite and augite models were used, respectively, for calculation in pressure fields >13 kbar and <13 kbar (Green et al., 2016).

The *P–T* pseudosection was constructed using the measured bulk composition (in mol%: Na_2O = 1.52, CaO = 13.61, K_2O = 0.19, FeO = 11.92, MgO = 13.90, Al_2O_3 = 9.26, SiO_2 = 43.91, TiO_2 = 1.21, H_2O = 3.29 and O_2 = 1.01) for the *P–T* range of 700–1000 °C and 0.2–2.5 GPa. In the calculated *P–T* range, the speculated peak mineral assemblage (M1) of Grt + Omp + Rt + Ilm is stable at *P–T* conditions of >1.8 GPa and >870 °C in the presence of melt (Fig. 13a). The isopleths of X_{Na} = 0.21–0.26 in omphacite have gentle slopes and are sensitive to change in pressure of ca. 1.4–1.8 GPa (Fig. 13b). The observed HT granulite-facies mineral assemblage (M2) of Grt (rim) + Cpx + Opx + Pl (Ca-rich) + Amp + Ilm is stable at *P–T* conditions of ca. 0.85–1 GPa and >830 °C in the presence of melt. The retrograde mineral assemblage (M3) of Amp + Bt + Cpx + Mt + Opx + Pl + Ilm is stable at *P–T* conditions of ca. 0.2–0.7 GPa and 700–855 °C in the presence of melt.

6.2. Conventional thermobarometry

Given the large stability fields of mineral assemblages corresponding to each metamorphic event in the Pseudosections, we also used conventional thermobarometry to calculate *P–T* conditions. The garnet-orthopyroxene-plagioclase-quartz thermobarometry (Lal, 1993) and amphibole-plagioclase thermometry (Holland and Blundy, 1994) with amphibole-plagioclase-quartz barometry (Bhadra and Bhattacharya, 2007) (Hbl-Pl-Q thermobarometry) are used to calculate the two-stage decompression metamorphic *P–T* conditions, respectively.

Using the compositions of orthopyroxene + plagioclase symplectite around garnet and garnet rim, the Grt-Opx-Pl-Q thermobarometry gives metamorphic conditions of 0.88–0.99 GPa and 875–920 °C in the stability field of Grt + Cpx + Opx + Pl + Amp + Ilm + L (Fig. 13b). By using the compositions of amphibole and plagioclase in the matrix, the Hbl-Pl-Q thermobarometry gives *P–T* conditions of 0.42–0.62 GPa and 774–822 °C in the two stability fields of Amp + Bt + Cpx + Mt + Opx + Pl + Ilm ± L (Fig. 13b).

7. Discussion

7.1. Early Paleozoic protolith and significance

Zircon U–Pb dating on inherited zircon cores of the HP eclogites gives a concordant age of ~ 450 Ma. The clear oscillatory zoning of these inherited cores with relatively high REE contents than their rims (see Figs. 8a and b, 9a and c, 10a and d) is consistent with their being of magmatic origin (e.g., Hoskin and Schaltegger, 2003). Thus, it is reasonable to suggest the Ordovician zircon core age represents the protolith crystallization age of the HP eclogites.

On the basis of bulk-rock compositional systematics, especially those of immobile incompatible elements (i.e., high field strength elements such as Nb, Ta, Zr, Hf, Ti and heavy REEs vs. mobile elements such as Rb, U and Pb), we reason that the protoliths of the HP eclogites are most likely seafloor basalts with an E-MORB signature (Figs. 6,7,14). They have flat or weakly enriched light REE patterns ($[La/Sm]_N$ = 0.92–1.56, $[Sm/Yb]_N$ = 1.07–1.58, where subscript N refers to normalization again primitive mantle values of Sun and McDonough, 1988) without depletion of Nb, Ta and Ti (Fig. 7). Moreover, the HP eclogites have positive $\varepsilon_{Hf}(t)$ of zircon magmatic cores, indicative of mantle source without important crustal assimilation at the time of the protolith magmatism. In addition, the systematic increases in FeO_T/MgO, TiO2, FeO_T and V (Figs. 6,15) with decreasing MgO is consistent with varying extent of basaltic magma evolution before Titanomagnetite on the liquidus (e.g., Niu, 2005). We should emphasize that the protoliths of the HP eclogites are unlikely to be arc basalts (IAB) because the latter would be highly depleted in water insoluble elements (e.g., Nb, Ta, Ti) and enriched in water-soluble elements (e.g., Ba, Rb, U, K, Sr, Pb) (e.g., Tatsumi and Eggins, 1995), but this is not the case. The apparent enrichment in Rb, U and Pb (Fig. 7) reflects fluid effects during metamorphism as reported in many other eclogites/blueschists of MORB protoliths such as in the Qilian orogen (e.g., Song et al., 2009), Variscan Sardinia orogen and Western Alps (e.g., Cruciani et al., 2017, 2018).

As we report here, Wang et al. (2017a) showed that the protoliths of the HP eclogites in ADM have positive bulk-rock $\varepsilon_{Nd}(t)$ values and similar geochemical affinities with E-MORB (Figs. 6, 7, 11 and 14), and their inherited magmatic zircons also indicate the Ordovician protolith age (~ 480–430 Ma). Moreover, the coeval mafic rocks (~ 457 Ma) have been reported near the Kharta area and felsic magmatism (~ 470–440 Ma) is also widespread in the Everest, Gyirong and Yadong areas within the GHS (e.g., Viskupic and Hodges, 2001; Cottle et al., 2009b; Visonà et al., 2010; Dong and Tian, 2019; Gao et al., 2019). We reason that the widespread Ordovician magmatism along the northern margin of the Indian continent is probably related to accretionary orogens of East Gondwana (e.g., Cawood and Buchan, 2007). Further study will be needed with more data to verify the E-MORB protolith interpretation for the HP eclogites.

7.2. Cenozoic metamorphism

7.2.1. *P–T* conditions of the central Himalayan eclogites

It is a challenge to obtain accurate peak metamorphic *P–T* conditions of the central Himalayan eclogites, most of which have been strongly overprinted by granulite-facies metamorphism (Lombardo and Rolfo, 2000; Groppo et al., 2007; Rolfo et al., 2008; Cottle et al., 2009b; Chakungal et al., 2010; Warren et al., 2011, Wang et al., 2017a, 2021; Li et al., 2019). In our samples, omphacite (inclusion) of peak eclogitic minerals has been preserved in the cores of porphyroblastic garnets. The compositions of eclogite-face garnet cores have been modified by diffusion during late granulite-facies metamorphism, representing a uniform composition pattern (Fig. 5a). Thus, the highest X_{Na} isopleth of omphacite gives the pressure condition of ca. 1.6–1.7 GPa in the omphacite stability field without plagioclase (Fig. 13b). Considering the observed breakdown of some omphacite inclusions (into Aug + Na-rich Pl) within garnet, this *P* condition is likely the minimum pressure constraint for eclogite-facies metamorphism. In the same studied area, Wang et al. (2021) obtained the pressure-peak condition of ~ 2 GPa by compositional isopleths of omphacite. For the subsequent metamorphic events M2 and M3 overprinting the eclogite metamorphism, the *P–T* conditions are constrained by overlapping fields of the mineral assemblage stability fields in the *P–T* pseudosection and using the conventional thermobarometry. For the event M2, HT-UHT granulite facies conditions of 0.88–0.99 GPa and 875–920 °C were constrained by the Grt-Opx-Pl-Q thermobarometry that is consistent with the mineral assemblage stability field (Grt + Cpx + Opx + Pl + Amp + Ilm + L) (Fig. 13b). For the event M3, the Hbl-Pl-Q thermobarometry yielded *P–T* conditions across two stability fields of Amp + Bt + Cpx + Mt + Opx + Pl + Ilm ± L. With this result, together with the petrography showing < 0.5 vol.% biotite in our samples, we suggest that the M3 *P–T* conditions are ca. 0.42–0.62 GPa and 800–820 °C (Fig. 13b).

Therefore, the eclogites in the central Himalaya experienced peak eclogite-facies metamorphism at >1.6 GPa, followed by HT-UHT decompression granulite-facies metamorphism (ca. 0.88–0.99 GPa and 875–920 °C) and by the subsequent cooling and decompression granulite-facies retrograde metamorphism (ca. 0.42–0.62 GPa and 800–820 °C).

7.2.2. Metamorphic time of the central Himalayan eclogites

Compared with older orogens, 1 Myr resolution for Himalayan metamorphism can be achieved by using typical microanalytical methods (with uncertainties of 2 %), whereas the same chronologic resolution in Paleozoic or Proterozoic orogens requires analytical methods that attain < 0.1 to 0.5 % uncertainties (e.g., Kohn et al., 2014). Our zircon U–Pb geochronology shows that most zircons of the HP eclogites have core–rim or core–mantle–rim structures, characteristic of mantle with patchy zoning and rim without zoning; other zircons have weak sector or fir-tree zoning, all suggesting zircons (including overgrown mantle, rim and metamorphic growth one) of metamorphic origin (Fig. 8; e.g., Corfu et al., 2003). Based on zircon REE characteristics, these metamorphic zircons give two group ages: (1) 17.9–15.3 Ma with a low-flat HREE pattern (green in Fig. 8b,d,e) and a weak or no Eu anomaly (Supplementary Table 6), (2) 14.8–13.3 Ma with a high-steep HREE pattern and a remarkable negative Eu anomaly (Figs. 9 and 10). We suggest that the timing of 17.9–15.3 Ma recorded by three samples is the granulite-facies metamorphic age for two reasons: (1) under the granulite-facies conditions, the existing garnets hold HREEs of the bulk rock, resulting in the low-flat HREE pattern of the zircons (e.g., Rubatto, 2002); (2) zircons forming under granulite-facies need to compete Eu with the existing and forming plagioclase, thus developing a strong negative Eu anomaly (cf. Rubatto, 2002 and references therein). We interpret that U–Pb system of minor zircons without a negative Eu anomaly (11/53) must have been completely reset during HT granulite facies metamorphism, but the host zircons preserve the REE characterisctis. Based on the *P*–*T* path (Fig. 13b), the HP eclogites in the central Himalaya experienced decompression cooling (Fig. 13b). During this process, garnet breaks down and plagioclase forms near the solidus, leading to abundant HREEs and Eu redistributed in the bulk-rock. Meanwhile, the coexisting and/or growing metamorphic zircons continue to grow with high HREE contents and a steep pattern with variably large negative Eu anomalies. Therefore, we interpret the 14.8–13.3 Ma age recorded by three samples as representing the retrograde decompression-cooling history.

Petrographically, titanite that rims ilmenite (both included in clinopyroxene-plagioclase symplectite) can be understood as formed by reactions such as: clinopyroxene + ilmenite → titanite + magnetite (Kohn, 2017) (Fig. 4k–m). Thus, the titanite U–Pb age of 15.4 Ma may indicate the onset of the retrograde decompression-cooling metamorphism. This age interpretation is consistent with the phase equilibria modelling (i.e., magnetite formation from M2 to M3; Fig. 13).

Therefore, our study suggests that the eclogites in the central Himalaya underwent HT-UHT granulite-facies metamorphism at ~ 17.9–15.3 Ma, followed by retrograde MP granulite-facies metamorphism at ~ 15.4–13.3 Ma.

7.2.3. Tectonic evolution

With all the observations, and discussion above, including the timing and *P*–*T* conditions of metamorphic events, we propose a clockwise *P*–*T*–*t* path that best describes the history of the HP eclogites in the central Himalaya. The *P*–*T*–*t* path is characterized by decompression from the HP eclogite facies to HT-UHT granulite facies at ~ 17.9–15.3 Ma and decompression-cooling across granulite facies to the solidus at ~ 14.8–13.3 Ma (Fig. 16).

The HP eclogites in the central Himalaya record a different evolution history from the UHP eclogites in the western Himalayan syntaxis. (1) They are not spatially associated with the ITSZ, but occur within the GHS or the MCTZ (Fig. 1); (2) they do not preserve UHP index minerals, but HP omphacite; and (3) they have strong granulite- and amphibolite-facies overprinting (e.g., Lombardo and Rolfo, 2000; Zhang et al., 2019). The most conspicuous feature of the HP eclogites is the clinopyroxene + plagioclase symplectite texture that has been reported in retrogressed eclogites in many orogenic belts, and is thought to be the replacement of omphacite by plagioclase and clinopyroxene formed during the transition from eclogite to HP granulite facies (e.g., Heinrich, 1982; O'Brien, 1990; Rubie, 1990; Joanny et al., 1991; Smelov and Beryozkin, 1993; Möller, 1998; Lombardo and Rolfo, 2000; Zhao et al., 2001). Based on the petrography, the samples in the Thongmön and Kharta areas of the central Himalaya have omphacite inclusions in garnet as well as the above-mentioned retrogressed eclogites textures, indicating the presence and significance of the peak HP eclogite-facies metamorphism (e.g., Li et al., 2019; Wang et al., 2021 and this study). Moreover, the HP eclogites in the central Himalaya underwent UHT granulite facies overprinting. Wang et al. (2021) suggested that the UHT conditions could be achieved in 30–40 Myrs after crustal thickening for rocks buried to > 60 km, which is consistent with our study. If the time of initial Indo-Asia continental collision is ~ 55 Ma (Hu et al., 2015), the HP eclogites must have begun to exhume at ~ 17.9–15.3 Ma, indicating their residence time in the deep crust for more than 30 m.y. The HP eclogites in the central Himalaya record long-lived burial and rapid exhumation histories.

8. Conclusion

(1) The HP eclogites of the GHS in the Thongmön and Kharta areas in the central

Himalaya preserve omphacite inclusions and textural evidence for peak eclogite-facies metamorphism and record HT-UHT granulite-facies and MP granulite-facies retrogressed overprints.

(2) The protoliths of the HP eclogites are seafloor tholeiitic basalts with E-MORB-like geochemistry, formed at ~ 450 Ma. These Ordovician basaltic protoliths show varying extent of fractional crystallization dominated magma evolution prior to titanomagnetite on the liquidus.

(3) The HP eclogites underwent decompression granulite-facies metamorphism at 17.9–15.3 Ma and subsequent decompression-cooling retrograde at 14.8–13.3 Ma, suggesting that the lower crustal materials of the Indian continent experienced a long-lived burial history since the India-Asia collision at ~ 55 Ma.

Acknowledgements

We thank two journal reviewers, Guest Editor Li-fei Zhang and Editor-in-Chief M. Santosh for their constructive comments, which have helped improve the quality of this paper. This study was co-supported by the National Natural Science Foundation of China (grants 41872070 and 91855210), the China Geological Survey (grant DD20190059) and Basic Science and Technology Research Funding of the Institute of Geology, CAGS (grant J2006). We thank Dr. Zhengbin Gou and Master student Guowei Liu for taking part in the field work; Chao Yu and Ying Liu for dating analysis.

Reference

Auzanneau, E., Schmidt, M.W., Vielzeuf, D., Connolly, J.A.D., 2010. Titanium in phengite: A geobarometer for high temperature eclogites. Contrib. Mineral. Petrol. 159, 1–24.

Bhadra, S., Bhattacharya, A., 2007. The barometer tremolite + tschermakite + 2 albite = 2 pargasite + 8 quartz: Constraints fromexperimental data at unit silica activity, with application to garnet-free natural assemblages. Am. Mineral. 92, 491–502.

Bhattacharyya, K., Mitra, G., 2009. A new kinematic evolutionary model for the growth of a duplex—An example from the Rangit duplex, Sikkim Himalaya, India. Gondwana Res. 16, 697–715.

Burchfiel, B.C., Chen, Z.L., Hodges, K.V., Liu, Y.P., Royden, L.H., Deng, C.R., Jiene, X., 1992. The South Tibetan Detachment System, Himalayan Orogen: Extension contemporaneous with and parallel to shortening in a Collisional Mountain Belt. Geol. Soc. Am. Spec. Pap. 269, 1–41.

Cawood, P.A., Johnson, M.R.W., Nemchin, A.A., 2007. Early Palaeozoic orogenesis along the Indian margin of Gondwana: Tectonic response to Gondwana assembly. Earth Planet. Sci. Lett. 255, 70–84.

Cawood, P.A., Buchan, C., 2007. Linking accretionary orogenesis with supercontinent assembly. Earth Sci. Rev. 82, 217–256.

Chakungal, J., Dostal, J., Grujic, D., Duchêne, S., Ghalley, S.K., 2010. Provenance of the Greater Himalayan Sequence: Evidence from mafic eclogite–granulites and amphibolites in NW Bhutan. Tectonophysics 480, 198–212.

Chin, E.J., Shimizu, K., Bybee, G.M., Erdman, M.E., 2018. On the development of the calc-alkaline and tholeiitic magma series: A deep crustal cumulate perspective. Earth Planet. Sci. Lett. 482, 277–287.

Chu, N.C., Taylor, R.N., Chavagnac, V., Nesbitt, R.W., Boella, R.M., Milton, J.A., German, C.R., Bayon, G., Burton, K., 2002. Hf isotope ratio analysis using multi-collector inductively coupled plasma mass spectrometry: An evaluation of isobaric interference corrections. J. Anal. At. Spectrom. 17, 1567–1574.

Coggon, R., Holland, T.J.B., 2002. Mixing properties of phengitic micas and revised garnet-phengite thermobarometers. J. Metamorph. Geol. 20, 683–696.

Corfu, F., Hanchar, J.M., Hoskin, P.W.O., Kinny, P., 2003. Atlas of zircon textures. Rev. Mineral. Geochem. 53, 469–500.

Corrie, S.L., Kohn, M.J., Vervoort, J.D., 2010. Young eclogite from the Greater Himalayan Sequence, Arun Valley, eastern Nepal: P–T–t path and tectonic implications. Earth Planet. Sci. Lett. 289, 406–416.

Cottle, J.M., Jessup, M.J., Newell, D.L., Searle, M.P., Law, R.D., Horstwood, M.S.A., 2007. Structural insights into the early stages of exhumation along an orogen-scale detachment: The South Tibetan detachment system, Dzakaa Chu section, Eastern Himalaya. J. Struct. Geol. 29, 1781–1797.

Cottle, J.M., Searle, M., P., Horstwood, M.S.A., Waters, D.J., 2009a. Timing of midcrustal metamorphism, melting, and deformation in the Mount Everest Region of Southern Tibet revealed by U(–Th)–Pb geochronology. J. Geol. 117, 643–664.

Cottle, J.M., Jessup, M.J., Newell, D.L., Horstwood, M.S.A., Noble, S.R., Parris, R.R., Waters, D.J., Searle, M.P., 2009b. Geochronology of granulitized eclogite from the Ama Drime Massif: Implications for the tectonic evolution of the South Tibetan Himalaya. Tectonics 28, TC1002.

Cruciani, G., Franceschelli, M., Puxeddu, M., 2017. U-, Pb-enrichment, Sr-depletion produced by water-rock interaction processes within the eclogitic oceanic crust of Ordovician age in NE Sardinia. Procedia Earth Plane. Sci. 17, 508–511.

Cruciani, G., Franceschelli, M., Scodina, M., Puxeddu, M., 2018. Garnet zoning in kyanite−bearing eclogite from golfo aranci: New data on the early prograde P-T evolution in NE Sardinia, Italy. Geol. J. 54, 190–205.

Dong, X., Tian, Z.L., 2019. Multistage tectono-thermal events in the Yadong area of the Himalayan orogenic belt: Evidence from zircon and monazite U-Th-Pb geochronology. Acta Petrol. Mineral. 38, 431–452.

Elhlou, S., Belousova, E., Griffin, W.L., Pearson, N.J., O'Reilly, S.Y., 2006. Trace element and isotopic composition of GJ-red zircon standard by laser ablation. Geochim. Cosmochim. Acta. 70, A158–A158.

Ewart, A., Collerson, K.D., Regelous, M., Wendt, J.I., Niu, Y.L., 1998. Geochemical evolution within the Tonga-Kermadec-Lau Arc-Backarc system: The role of varying mantle wedge composition in space and time. J. Petrol. 39, 331–368.

Florence, F.P., Spear, F.S., 1991. Effects of diffusional modification of garnet growth zoning on P-T path calculations. Contrib. Mineral. Petrol. 107, 487–500.

Gao, L.E., Zeng, L.S, Hu, G.Y, Wang, Y.Y., Wang, Q., Guo, C.L, Hou, K.J., 2019. Early Paleozoic magmatism along the northern margin of East Gondwana.

Lithos 334–335, 25–41.

Goscombe, B., Gray, D., Hand, M., 2006. Crustal architecture of the Himalayan metamorphic front in eastern Nepal. Gondwana Res. 10, 232–255.

Goscombe, B., Hand, M., 2000, Contrasting P-T paths in the eastern Himalaya, Nepal: Inverted isograds in a paired metamorphic mountain belt. J. Petrol. 41, 1673–1719.

Green, E.C.R., Holland, T.J.B., Powell, R., 2007. An order-disorder model for omphacitic pyroxenes in the system jadeite-diopside-hedenbergite-acmite, with applications to eclogitic rocks. Am. Mineral. 92, 1181–1189.

Green, E.C.R., White, R.W., Diener, J.F.A., Powell, R., Holland, T.J.B., Palin, R.M., 2016. Activity–composition relations for the calculation of partial melting equilibria in metabasic rocks. J. Metamorph. Geol. 34, 845–869.

Groppo, C., Lombardo, B., Rolfo, F., Pertusati, P., 2007. Clockwise exhumation path of granulitized eclogites from the Ama Drime range (Eastern Himalayas). J. Metamorph. Geol. 25, 51–75.

Groppo, C., Rolfo, F., Lombardo, B., 2009. P-T evolution across the Main Central Thrust Zone (Eastern Nepal): Hidden discontinuities revealed by petrology. J. Petrol. 50, 1149–1180.

Grujic, D., Warren, C.J., Wooden, J.L., 2011. Rapid synconvergent exhumation of Miocene-aged lower orogenic crust in the eastern Himalaya. Lithosphere 3, 346–366.

Guillot, S., Maheo, G., de Sigoyer, J., Hattori, K.H., Pecher, A., 2008. Tethyan and

Indian subduction viewed from the Himalayan high- to ultrahigh-pressure metamorphic rocks. Tectonophysics 451, 225–241.

Heinrich, C.A., 1982. Kyanite-eclogite to amphibolite facies evolution of hydrous mafic and pelitic rocks, Adula Nappe, central Alps. Contrib. Mineral. Petrol. 81, 30–38.

Holland, T.J.B., Blundy, J.D., 1994. Non-ideal interactions in calcic amphiboles and their bearing on amphibole–plagioclase thermometry. Contrib. Mineral. Petrol. 116, 433–447.

Holland, T.J.B., Powell, R., 1998. An internally consistent thermodynamic data set for phases of petrological interest. J. Metamorph. Geol. 16, 309–343.

Holland, T.J.B., Powell, R., 2003. Activity–composition relations for phases in petrological calculations: An asymmetric multicomponent formulation. Contrib. Mineral. Petrol. 145, 492–501.

Holland, T.J.B., Powell, R., 2011. An improved and extended internally consistent thermodynamic dataset for phases of petrological interest, involving a new equation of state for solids. J. Metamorph. Geol. 29, 333–383.

Hoskin, P.W.O., Schaltegger, U., 2003. The composition of zircon and igneous and metamorphic petrogenesis. Rev. Mineral. Geochem. 53, 27–62.

Hou, K.J., Li, Y.H., Zou, T.R., Qu, X.M., Shi, Y.R., Xie, G.Q., 2007. Laser ablation-MC-ICP-MS technique for Hf isotope microanalysis of zircon and its geological applications. Acta Petrol. Sin. 23, 2595–2604.

Hu, X.M, Garzanti, E., Moore, T., Raffi, I., 2015. Direct stratigraphic dating of India-

Asia collision onset at the Selandian (middle Paleocene, 59 ± 1 Ma). Geology 43, 859–862.

Imayama, T., Takeshita, T., Arita, K., 2010. Metamorphic P–T profile and P–T path discontinuity across the far-eastern Nepal Himalaya: Investigation of channel flow models. J. Metamorph. Geol. 28, 527–549.

Irvine, T.N., Baragar, W.R.A., 1971. A guide to the chemical classification of common volcanic rocks. Can. J. Earth Sci. 8, 523–548.

Jessup, M.J., Newell, D.L., Cottle, J.M., Berger, A.L., Spotila, J.A., 2008. Orogen-parallel extension and exhumation enhanced by denudation in the trans-Himalayan Arun River gorge, Ama Drime Massif, Tibet–Nepal. Geology 36, 587–590.

Joanny, V., van Roermund, H. Lardeaux, J.M., 1991. The clinopyroxene/plagioclase symplectite in retrograde eclogites: A potential geothermobarometer. International J. Earth Sci. 80, 303–320.

Kali, E., Leloup, P.H., Arnaud, N., Mahéo, G., Liu, D., Boutonnet, E., Van Der Woerd, J., Liu, X., Liu-Zeng, J., and Li, H., 2010, Exhumation history of the deepest central Himalayan rocks, Ama Drime range: Key pressure-temperature-deformation-time constraints on orogenic models. Tectonics 29, TC2014.

Kellett, D.A., Cottle, J.M., Smit, M., 2014. Eocene deep crust at Ama Drime, Tibet: Early evolution of the Himalayan orogen. Lithosphere 6, 220–229.

Kellett, D.A., Grujic, D., Warren, C., Cottle, J., Jamieson, R., Tenzin, T., 2010, Metamorphic history of a syn-convergent orogen-parallel detachment: The

South Tibetan detachment system, Bhutan Himalaya. J. Metamorph. Geol. 28, 785–808.

Kohn, M.J., 2008. P-T-t data from central Nepal support critical taper and repudiate large-scale channel flow of the Greater Himalayan sequence. Geol. Soc. Am. Bull. 120, 259–273.

Kohn, M.J., 2014. Himalayan metamorphism and its tectonic implications. Annu. Rev. Earth Planet. Sci. 42, 381–419.

Kohn, M.J., 2017. Titanite Petrochronology. Rev. Mineral. Geochem. 83, 419–441.

Kohn, M.J., Spear, F., 2000. Retrograde net transfer reaction insurance for pressure-temperature estimates. Geology 28, 1127–1130.

Lal, R.K., 1993. Internally consistent recalibrations of mineral equilibria for geothermobarometry involving garnet–orthopyroxene–plagioclase–quartz assemblages and their application to the South Indian granulites. J. Metamorph. Geol. 11, 855–866.

Leloup, P.H., Mahéo, G., Arnaud, N., Kali, E., Boutonnet, E., Liu, D.Y., Liu, X.H., Li, H.B., 2010. The South Tibet detachment shear zone in the Dinggye area Time constraints on extrusion models of the Himalayas. Earth Planet. Sci. Lett. 292, 1–16.

Li, D.W., Liao, Q.N., Yuan, Y.M.,Wan, Y.S., Liu, D.M., Zhang, X.H., Yi, S.H., Cao, S.Z., Xie, D.F., 2003. SHRIMP U–Pb zircon geochronology of granulites at Rimana (Southern Tibet) in the central segment of Himalayan Orogen. Chin. Sci. Bull. 48, 2647–2650.

Li, Q.Y., Zhang, L.F., Fu, B., Bader, T., Yu, H.L., 2019. Petrology and zircon U–Pb dating of well-preserved eclogites from the Thongmön area in central Himalaya and their tectonic Implications. J. Metamorph. Geol. 37, 203–226.

Li, X.H., 1997. Geochemistry of the Longsheng Ophiolite from the southern margin of Yangtze Craton, SE China. Geochem. J. 31, 323–337.

Liu, Y., Siebel, W., Massonne, H.J., Xiao, X.C., 2007. Geochronological and petrological constraints for tectonic evolution of the Central Greater Himalayan Sequence in the Kharta Area, Southern Tibet. J. Geol. 115, 215–230.

Lombardo, B. Rolfo, F., 2000. Two contrasting eclogite types in the Himalayas: Implications for the Himalayan orogeny. J. Geodyn. 30, 37–60.

Lombardo, B., Pertusati, P., Rolfo, F., VisonaÁ, D., 1998. First report of eclogites from the Eastern Himalaya: Implications for the Himalayan orogeny. Memorie di Scienze Geologiche dell'Università di Padova 50, 67–68.

Ludwig, K.R., 2003. ISOPLOT 3.00: A Geochronological Toolkit for Microsoft Excel. Berkeley Geochronology Center, Berkeley, CA.

Miyashiro, A., 1974. Volcanic rock series in island arcs and active continental margins. Am. J. Sci. 274, 321–355.

Möller, C., 1998. Decompressed eclogites in the Sveconorwegian (Grenvillian) orogen of SW Sweden: Petrology and tectonic implications. J. Metamorph. Geol., 16, 641–656.

Morimoto, N., 1988. Nomenclature of pyroxenes. Mineral. Mag. 52, 535–550.

Najman, Y., Appel, E., Boudagher-Fadel, M., Bown, P., Carter, A., Garzanti, E., Godin, L., Han, J.T., Liebke, U., Oliver, G., Parrish, R., Vezzoli, G., 2010. Timing of India-Asia collision: Geological, biostratigraphic, and palaeomagnetic constraints. J. Geophys. Res. 115, B12416.

Niu, Y., O'Hara, M.J., 2003. Origin of ocean island basalts: A new perspective from petrology, geochemistry, and mineral physics considerations. J. Geophys. Res. 108(B4), 2209.

Niu, Y.L., Regelous, M., Wendt, J.I., Batiza, R., O'Hara, M.J., 2002. Geochemistry of near-EPR seamounts: Importance of source vs. process and the origin of enriched mantle component. Earth Planet. Sci. Lett. 199, 327–345.

O'Brien, P. J., 1990. Eclogite formation and distribution in the European Variscides. In: Eclogite Facies Rocks (ed. Carswell, D. A.), pp. 204–224. Blackie, Glasgow and London.

Paton, C., Woodhead, J.D., Hellstrom, J.C., Hergt, J.M., Greig, A., Maas, R., 2010. Improved laser ablation U-Pb zircon geochronology through robust downhole fractionation correction. Geochem. Geophys. Geosyst. 11, Q0AA06.

Rolfo, F., Carosi, R., Monotomoli, C., Visona, D., 2008. Discovery of granuilitized eclogite in North Sikkim expands the Eastern Himalaya high pressure province. Extended Abstracts: 23rd Himalaya-Karakoram-Tibet Workshop, India.

Rubatto, D., 2002. Zircon trace element geochemistry: Partitioning with garnet and the link between U–Pb ages and metamorphism. Chem. Geol. 184, 123–138.

Rubie, D.C., 1990. Role of kinetics in the formation and preservation of eclogites. In: Eclogite Facies Rocks (ed. Carswell, D. A.), pp. 111–140. Blackie, Glasgow.

Schelling, D., 1992. The tectonostratigraphy and structure of the eastern Nepal Himalaya. Tectonics 11, 925–943.

Searle, M.P., Law, R.D., Godin, L., Larson, K.P., Streule, M.J., Cottle, J.M., Jessup, M.J., 2008. Defining the Himalayan Main Central Thrust in Nepal. J. Geol. Soc. 165, 523–534.

Searle, M.P., Simpson, R.L., Law, R.D., Parrish, R.R., Waters, D.J. 2003. The structural geometry, metamorphic and magmatic evolution of the Everest massif, High Himalaya of Nepal-South Tibet. J. Geol. Soc. 160, 345–366.

Smelov, A.P., Beryozkin, V.I., 1993. Retrograded eclogites in the Olekma granite–greenstone region, Aldan Shield, Siberia. Precambrian Res. 62, 419–430.

Spandler, C., Hammerli, J., Sha, P., Hilbert-Wolf, H., Hu, Y., Roberts, E., Schmitz, M., 2016. MKED1: A new titanite standard for in situ analysis of Sm–Nd isotopes and U–Pb geochronology. Chem. Geol. 425, 110–126.

Spear, F.S., 1991. On the interpretation of peak metamorphic temperatures in light of garnet diffusion during cooling. J. Metamorph. Geol. 9, 379–388.

Stacey, J.S., Kramers, J.D., 1975. Approximation of terrestrial lead isotope evolution by a two-stage model. Earth Planet. Sci. Lett. 26, 207–221.

Sun, J.F., Yang, J.H., Wu, F.Y., Xie, L.W., Yang, Y.H., Liu, Z.C., Li, X.H., 2012. In situ U–Pb dating of titanite by LA-ICPMS. Chin. Sci. Bull. 57, 2506–2516.

Sun, S.S., McDonough, W.F., 1989. Chemical and isotope systematics of oceanic basalts: Implications for mantle composition and processes. In: Saunders, A.D. (Ed.), Magmatism in Ocean Basins. Geological Society Publication, 42, pp. 313–345.

Tatsumi, Y., Eggins, S., 1995. Subduction Zone Magmatism. Blackwell Science, 231.

Tera, F., Wasserburg, G.J., 1972. U-Th-Pb systematics in three Apollo 14 basalts and the problem of initial Pb in lunar rocks. Earth Planet. Sci. Lett. 14, 281–304.

Viskupic, K., Hodges, K.V., 2001. Monazite–xenotime thermochronometry: Methodology and an example from the Nepalese Himalaya. Contrib. Mineral. Petrol. 141, 233–247.

Visonà, D., Rubatto, D., Villa, I. M., 2010. The mafic rocks of Shao La (Kharta, S. Tibet): Ordovician basaltic magmatism in the greater Himalayan crystallines of central-eastern Himalaya. J. Asian Earth Sci. 3, 14–25.

Wang, J.M., Rubatto, D., Zhang, J.J., 2015. Timing of Partial Melting and Cooling across the Greater Himalayan Crystalline Complex (Nyalam, Central Himalaya): In-sequence Thrusting and its Implications. J. Petrol. 56, 1677–1702.

Wang, J.M., Wu, F.Y., Rubatto, D., Liu, S.R., Zhang, J.J., Liu, X.C., Yang, L., 2017b. Monazite behaviour during isothermal decompression in pelitic granulites: A case study from Dinggye, Tibetan Himalaya. Contrib. to Mineral. Petrol. 172, 81.

Wang, J.M., Zhang, J.J., Wang, X.X., 2013. Structural kinematics, metamorphic P-T profiles and zircon geochronology across the Greater Himalayan Crystalline Complex in south-central Tibet: Implication for a revised channel flow. J. Metamorph. Geol. 31, 607–628.

Wang, J.M., Lanari, P., Wu, F.Y., Zhang, J.J., Khanal, G.P., Yang, L., 2021. First evidence of eclogites overprinted by ultrahigh temperature metamorphism in

Everest East, Himalaya: Implications for collisional tectonics on early earth. Earth Planet. Sci. Lett. 558, 116760.

Wang, Y.H., Zhang, L.F., Zhang, J.J., Wei, C.J., 2017a. The Youngest eclogite in central Himalaya: P–T path, U–Pb zircon age and its tectonic implication. Gondwana Res., 41, 188–206.

Warren, C. J., Grujic, D., Kellett, D. A., Cottle, J., Jamieson, R. A., Ghalley, K. S., 2011. Probing the depths of the India–Asia collision: U–Th–Pb monazite chronology of granulites from NW Bhutan. Tectonics 30, TC2004.

White, R.W, Powell, R., Holland, T.J.B., Johnson, T.E., Green, E.C.R., 2014. New mineral activity–composition relations for thermodynamic calculations in metapelitic systems. J. Metamorph. Geol. 32, 261–286.

White, R.W., Powell, R., Holland, T.J.B., Worley, B.A., 2000. The effect of TiO_2 and Fe_2O_3 on metapelitic assemblages at greenschist and amphibolite facies conditions: mineral equilibria calculations in the system K_2O–FeO–MgO–Al_2O_3–SiO_2–H_2O–TiO_2–Fe_2O_3. J. Metamorph. Geol. 18, 497–511.

Winchester, J.A., Floyd, P.A., 1976. Geochemical magma type discrimination: Application to altered and metamorphosed basic igneous rocks. Earth Planet. Sci. Lett. 28, 459–469.

Winter, J.D., 2001. An introduction to igneous and metamorphic petrology. pp. 1–697. New York, NY: Prentice Hall.

Xiang, H., 2020. GeoPS: an interactive visualization tool for thermodynamic modeling of phase equilibria. https://doi.org/10.1002/essoar.10502553.1

Yin, A., 2006. Cenozoic tectonic evolution of the Himalayan orogen as constrained by along-strike variation of structural geometry, exhumation history, and foreland sedimentation. Earth Sci. Rev. 76, 1–131.

Yin, A., Harrison, T.M., 2000. Geologic evolution of the Himalayan-Tibetan orogen. Annu. Rev. Earth Planet. Sci. 28, 211–280.

Yu, C., Yang, Z.M., Zhou, L.M., Zhang, L.L., Li, Z.Q., Zhao, M., Zhang, J.Y., Chen, W.Y., Suo, M.S., 2019. Impact of laser focus on accuracy of U-Pb dating of zircons by LA-ICPMS. Mineral Deposits, 38, 21–28.

Zhang, Z.M., Ding, H.X., Dong, X., Tian, Z.L., 2019. Two contrasting eclogite types in the Himalayan Orogen and differential subduction of Indian continent. Earth Sci. 44, 1602–1619.

Zhao, G.C., Cawood, P. A., Wilde, S. A., Lu, L.Z., 2001. High-Pressure Granulites (Retrograded Eclogites) from the Hengshan Complex, North China Craton: Petrology and Tectonic Implications. J. Petrol. 42, 1141–1170.

Supplementary data to this article:

Supplementary Table 1 Representative electron probe analyses of garnet from the HP eclogite (sample T15-5-7) in the central Himalaya

Supplementary Table 2 Representative electron probe analyses of pyroxene from the HP eclogite (sample T15-5-7) in the central Himalaya

Supplementary Table 3 Representative electron probe analyses of plagioclase from the HP eclogite (sampleT15-5-7) in the central Himalaya

Supplementary Table 4 Representative electron probe analyses of amphibole from the HP eclogite (sample T15-5-7) in the central Himalaya

Supplementary Table 5 Bulk-rock major and trace element data of the HP eclogites in the central Himalaya

Supplementary Table 6 Zircon LA-ICP-MS U–Pb age and trace element data of the HP eclogites in the central Himalaya

Supplementary Table 7 Zircon Lu-Hf isotopes data of the HP eclogites in the central Himalaya

Supplementary Table 8 Titanite LA-ICP-MS U–Pb age data of the HP eclogites in the central Himalaya

Figure captions:

Fig. 1. Sketch geological map of the central Himalaya (modified after Schelling, 1992; Goscombe and Hand, 2000; Goscombe et al., 2006; Bhattacharyya and Mitra, 2009; Kali et al., 2010; Kellett et al., 2010; Grujic et al., 2011), showing locations of HP eclogite outcrops reported in the literature: Laya of NW Bhutan (Grujic et al., 2011), Sikkim of India (Rolfo et al., 2008), Ama Drime Massif (ADM, e.g., Lombardo et al., 1998; Groppo et al., 2007; Cottle et al., 2009a, b; Kellett et al., 2014; Wang et al., 2017a) and Thongmön (Cottle et al., 2009a, b; Li et al., 2019; Wang et al., 2021) of China, Arun Valley of Nepal (Corrie et al., 2010). Inset shows the region in the context of the Himalaya-Tibet orogen. Abbreviations: MBT = Main Boundary Thrust, MFT = Main Frontal Thrust, and STDS = South Tibetan Detachment System.

Fig. 2. Simplified geological map of the Dinggye region (see Fig. 1), central Himalaya (modified after Wang et al., 2017b), showing the locations and ages of HP eclogites and outcrops of the Ordovician mafic rocks reported in the literature: [1] Visonà et al. (2010), [2] Li et al. (2003), [3] Cottle et al. (2009a), [4] Li et al. (2019), [5] Wang et al. (2021), [6] Cottle et al. (2009b), [7] Kellett et al. (2014), [8] Wang et al. (2017a). Red and green values refer to protolithic/magmatic ages and metamorphic ages (Ma), respectively.

Fig. 3. Field photographs of the HP eclogites in the Thongmön ([2-5] in Fig. 2) and Kharta ([1, 6-7] in Fig. 2) areas. (a) a HP eclogite block "hosted" in gneiss and schist. (b) HP eclogite lenses and their granulitized equivalents "hosted" in paragneiss.

Fig. 4. BSE images (a, e, f, i and j), elemental maps (b, c, h, l and m) and photomicrographs (d, g and k) of the representative HP eclogites in the central Himalaya. (a) preservation of primary omphacite and rutile in the core of a garnet crystal, indicating prior eclogite-facies metamorphism. The garnet rims showing replacement by symplectite of amphibole + Ca-rich plagioclase. Fine-grained magnetite is scattered in amphiboles in the matrix. (b) and (c) are Na and Ca X-ray mappings of the Fig. 4a view field with element content increasing from cold to warm color as in Fig. 4h, l and m. (d) and (e) Showing retrograde transition from eclogite to HP granulite facies: A symplectite of amphibole + Na-rich plagioclase aggregates

replacing precursor omphacite. (f) MP granulite-facies retrogression: Amphiboles replace symplectite of clinopyroxene-plagioclase. (g) HP eclogite consists of garnet, clinopyroxene, orthopyroxene, plagioclase, quartz, amphibole. (h) Ca X-ray mapping of Fig. 4g field. (i) The porphyroblastic garnet has inclusions of clinopyroxene, Na-rich plagioclase, quartz, rutile and ilmenite in its core, which could be retrogressive product of eclogite-facies mineral assemblage. (j) Decompressing mineral reactions: A Ca-rich plagioclase + orthopyroxene ± amphibole symplectite replaces garnet and quartz. (k) Titanite rimming ilmenite occurs in symplectite of clinopyroxene + plagioclase (see l and m). (l) and (m) Ca and Ti X-ray mappings of Fig. 4k view field. Mineral abbreviations: Amp-amphibole, Ap-apatite, Cpx-clinopyroxene, Grt-garnet, Ilm-ilmenite, Mt-magnetite, Omp-omphacite, Pl-plagioclase, Opx-orthopyroxene, Qz-quartz, Rt-rutile, Ttn-titanite.

Fig. 5. (a) Major element zoning profile of garnet as shown in Fig. 4a. (b) and (c) Representative compositions of pyroxene within the HP eclogites in the central Himalaya (Morimoto, 1988).

Fig. 6. Classification diagrams of the HP eclogites in the central Himalaya. (a) Nb/Y vs. Zr/Ti diagram (Winchester and Floyd, 1976). (b) (Na_2O + K_2O)–FeO_t–MgO (wt.%) diagram (AFM) (Irvine and Baragar, 1971). (c) FeO_t/MgO vs. TiO_2 (wt.%) diagram (Miyashiro, 1974). Literature data for ~ 457 Ma mafic rocks near the Kharta area and the ADM HP eclogites are from Visonà et al. (2010) and Wang et al. (2017a),

showed in Fig. 2 [1] and [8] respectively.

Fig. 7. Ocean crust-normalized REE (a) and ocean crust-normalized multi-element (b) patterns for the HP eclogites in the central Himalaya. Average ocean crust, oceanic gabbro and island arc tholeiitic basalt compositions are from Niu and O'Hara (2003) and Ewart et al. (1998); Data of E-MORB and OIB are from Sun and McDonough (1989). Literature data for ~ 457 Ma mafic rocks near the Kharta area and the ADM HP eclogites are from Visonà et al. (2010) and Wang et al. (2017a), respectively.

Fig. 8. CL images of the representative zircons of the HP eclogites in the central Himalaya. The circles are the analytical spots with ages in Ma. Red open circles represent the analysis domain on zircon cores (Fig. 8a and b), giving the protolith ages. Green open circles represent the analysis domain of overgrown rims (Fig. 8a and b) or mantles (Fig. 8c), giving the HT granulite-facies metamorphic ages. Blue open circles represent the analysis domain on metamorphic growth zircons (Fig. 8b) or overgrown rims (Fig. 8c and d), giving the retrograde MP granulite-facies metamorphic ages. Red dotted-line represent domains of residual zircon cores with abundant inclusions, C, M and R represent core, mantle and rim domains of zircons (Fig. 8c and d).

Fig. 9. Zircon U–Pb concordia diagrams for the HP eclogites in the central Himalaya. Red ellipses represent the analyses on zircon cores (Fig. 8a and b), giving the protolith

ages (Fig. 9a and c). Green ellipses represent the analyses on overgrown rims (Fig. 8a and b) or mantles (Fig. 8c), giving the HT granulite-facies metamorphic ages (Fig. 9b, d and e). Blue ellipses represent the analyses on metamorphic growth zircons (Fig. 8b) or overgrown rims (Fig. 8c and d), giving the retrograde MP granulite-facies metamorphic ages (Fig. 9d−f).

Fig. 10. Chondrite-normalized REE patterns of zircons of the HP eclogites in the central Himalaya. Data of the chondrite are from Sun and McDonough (1989). Red lines are REE patterns of analyses on zircon cores (Fig. 8a and b) of the protolith magmatic crystallization (Fig. 10a and c). Green lines are REE patterns of analyses on zircon rims (Fig. 8a and b) or mantles (Fig. 8c) of the HT granulite-facies metamorphic overgrown (Fig. 10b, d and e). Blue lines are REE patterns of analyses on metamorphic zircons (Fig. 8b) or rims (Fig. 8c and d) of the retrograde MP granulite-facies metamorphic growth (Fig. 10d−f).

Fig. 11. U–Pb age vs. zircon $\varepsilon_{Hf}(t)$ (left) and bulk rock $\varepsilon_{Nd}(t)$ (right) diagram for the HP eclogites and related rocks from the central Himalaya. Average N-MORB composition of $\varepsilon_{Nd}(t) = 10.04$ is from Niu et al. (2002). Literature data for ~ 457 Ma mafic rocks near the Kharta area and the ADM HP eclogites are from Visonà et al. (2010) and Wang et al. (2017a), respectively. Abbreviations: DM = depleted mantle.

Fig. 12. Titanite U–Pb concordia diagrams of the HP eclogite in the central Himalaya.

Fig. 13. *P–T* pseudosections for the HP eclogite (sample T15-5-7) in the central Himalaya, calculated for the system NCKFMASHTO (+ Ilm) using the measured bulk composition. In (a) Phase assemblage fields are shaded more heavily according to variance. Omphacitic pyroxene (Di) and augite (Aug) were used for labelling in the HP field (>13 kbar) and medium- to low-pressure fields (<13 kbar), respectively, and the omphacitic pyroxene with a jadeite component larger than 20% was marked as omphacite (Omp). The pseudosection (b) is contoured with isopleths of X_{Na} (Omp) in omphacite using blue lines and vol% biotite using brown lines. Translucent rose-red rectangles represent *P–T* conditions for M2 and M3 calculated using conventional thermobarometry. The dark rose-red fields are overlapping fields of the mineral assemblage stability field and conventional thermobarometry, finally limiting the *P–T* conditions of M2 and M3 stages. Mineral abbreviations: Amp-amphibole, Aug-augite, Bt-biotete, Di-diopside, Ep-epidote, Grt-garnet, Ilm-ilmenite, Ma-margarite, Ms-muscovite, Mt-magnetite, Omp-omphacite, Pl-plagioclase, Opx-orthopyroxene, Qz-quartz, Rt-rutile, Ttn-titanite, Zo-zoisite, L-liquid.

Fig. 14. Th/Yb vs. Ta/Yb diagram for of the HP eclogites and related rocks from the central Himalaya. Data of E-MORB, N-MORB and OIB are from Sun and McDonough (1989). The literature data for ~ 457 Ma mafic rocks near the Kharta area and the ADM HP eclogites are from Visonà et al. (2010) and Wang et al. (2017a), respectively.

Fig. 15. MgO variation diagrams of FeO_t, TiO_2, and V for the HP eclogites in the central Himalaya.

Fig. 16. Integrated metamorphic *P*–*T* paths of the HP eclogites in the central Himalaya (modified after Li et al., 2019). The facies boundaries are modified after Winter (2001). The dark rose-red fields are *P*–*T* conditions of M2 and M3 stages that overlap the fields of the mineral assemblage stability field and conventional thermobarometry.

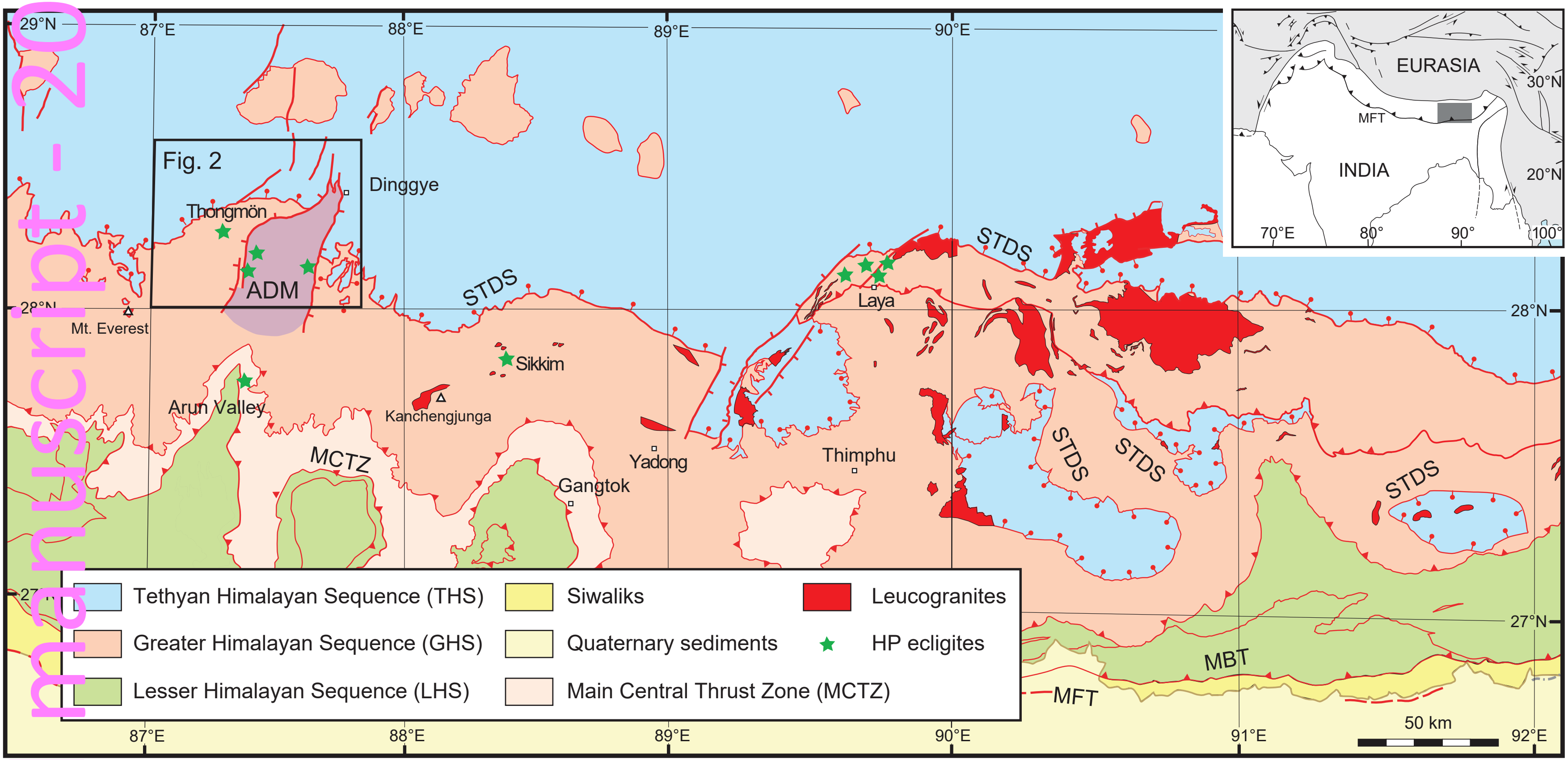
29°N
87°E
88°E
89°E
90°E
Fig. 2
Dinggye
Thongmön
ADM
28°N
Mt. Everest
STDS
Laya
Sikkim
Arun Valley
Kanchengjunga
MCTZ
Yadong
Thimphu
Gangtok
STDS
STDS
STDS
28°N
27°N
MBT
MFT
50 km
87°E
88°E
89°E
90°E
91°E
92°E
EURASIA
30°N
MFT
INDIA
20°N
70°E
80°
90°
100°
Tethyan Himalayan Sequence (THS)
Greater Himalayan Sequence (GHS)
Lesser Himalayan Sequence (LHS)
Siwaliks
Quaternary sediments
Main Central Thrust Zone (MCTZ)
Leucogranites
HP ecligites

Figure 1

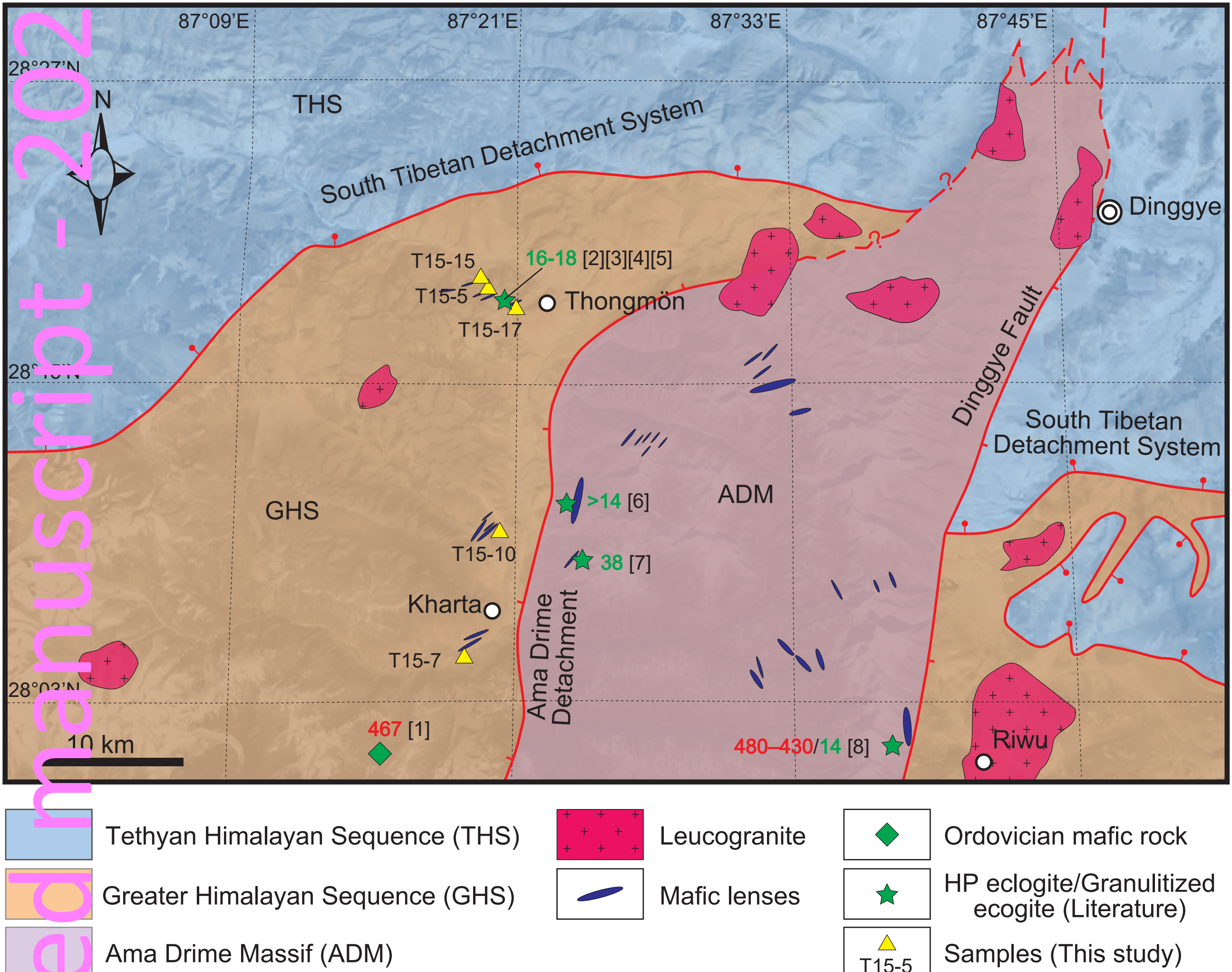
87°09'E
87°21'E
87°33'E
87°45'E
28°27'N
28°15'N
28°03'N
N
THS
South Tibetan Detachment System
T15-15
16-18 [2][3][4][5]
T15-5
T15-17
Thongmön
Dinggye
Dinggye Fault
South Tibetan Detachment System
ADM
>14 [6]
38 [7]
GHS
T15-10
Kharta
T15-7
Ama Drime Detachment
467 [1]
480–430/14 [8]
Riwu
10 km
Tethyan Himalayan Sequence (THS)
Greater Himalayan Sequence (GHS)
Ama Drime Massif (ADM)
Leucogranite
Mafic lenses
Ordovician mafic rock
HP eclogite/Granulitized ecogite (Literature)
T15-5
Samples (This study)

Figure 2

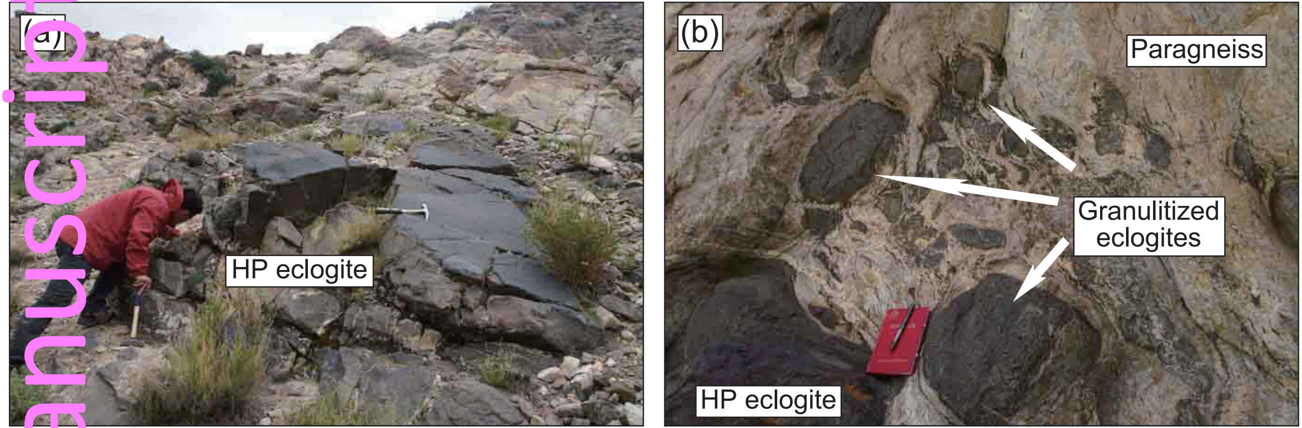
(a)
HP eclogite
(b)
Paragneiss
Granulitized eclogites
HP eclogite

Figure 3

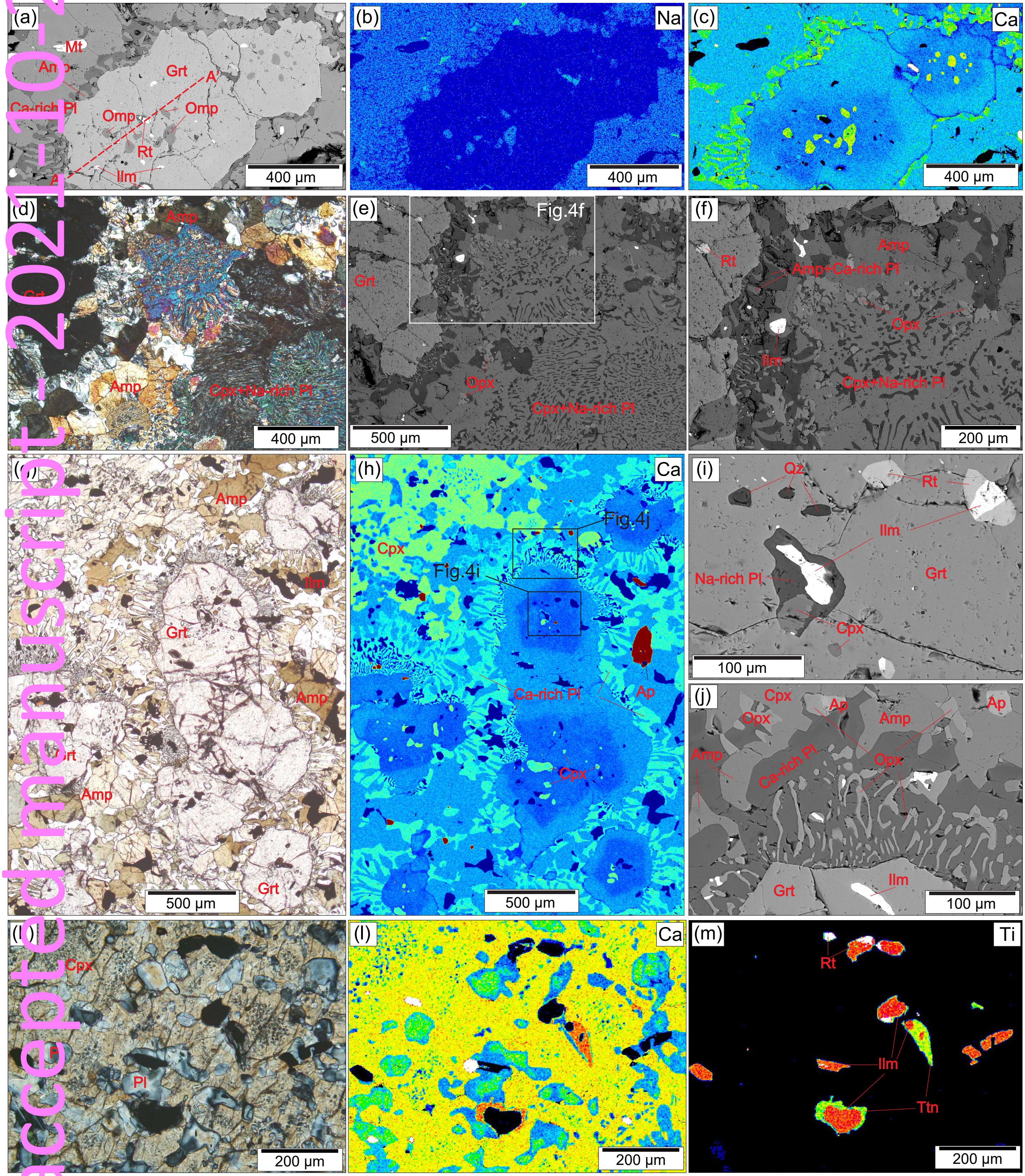

(a)
Mt
Amp
Grt
A'
Ca-rich Pl
Omp
Omp
Rt
Ilm
A
400 µm
(b)
Na
400 µm
(c)
Ca
400 µm
(d)
Amp
Amp
Cpx+Na-rich Pl
400 µm
(e)
Fig.4f
Grt
Opx
Cpx+Na-rich Pl
500 µm
(f)
Rt
Amp
Amp+Ca-rich Pl
Opx
Ilm
Cpx+Na-rich Pl
200 µm
Amp
Ilm
Grt
Amp
Amp
Grt
500 µm
(h)
Ca
Cpx
Fig.4j
Fig.4i
Ca-rich Pl
Ap
Cpx
500 µm
(i)
Qz
Rt
Ilm
Na-rich Pl
Grt
Cpx
100 µm
(j)
Cpx
Ap
Ap
Opx
Amp
Amp
Ca-rich Pl
Opx
Grt
Ilm
100 µm
Cpx
Pl
200 µm
(l)
Ca
200 µm
(m)
Ti
Rt
Ilm
Ttn
200 µm

Figure 4

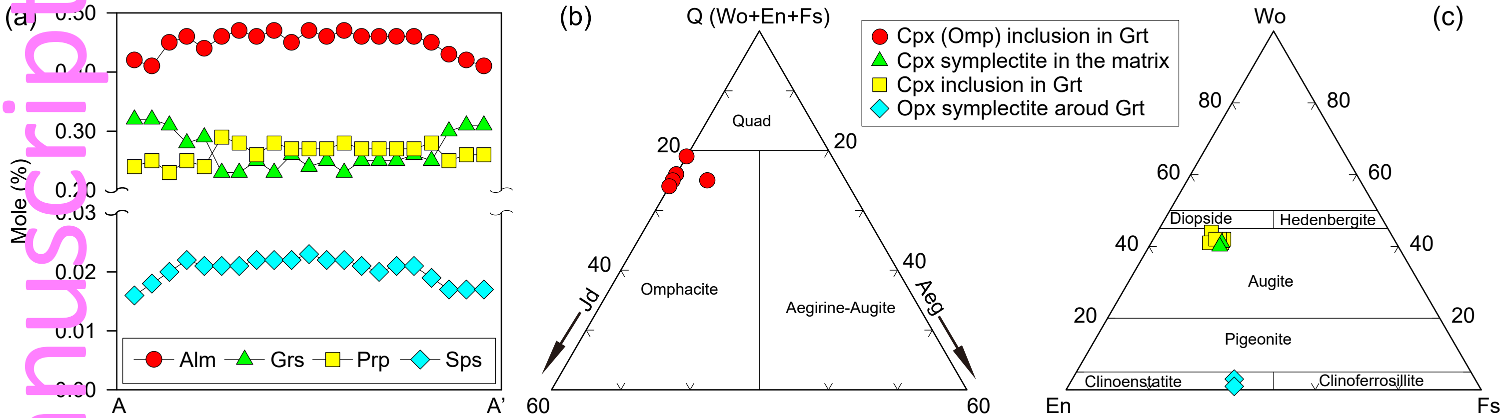

(a)
0.50
0.40
0.30
0.20
0.03
0.02
0.01
0.00
Mole (%)
Alm
Grs
Prp
Sps
A
A'
(b)
Q (Wo+En+Fs)
Quad
Omphacite
Aegirine-Augite
Jd
Aeg
20
40
60
Cpx (Omp) inclusion in Grt
Cpx symplectite in the matrix
Cpx inclusion in Grt
Opx symplectite aroud Grt
(c)
Wo
En
Fs
80
60
40
20
Diopside
Hedenbergite
Augite
Pigeonite
Clinoenstatite
Clinoferrosillite

Figure 5

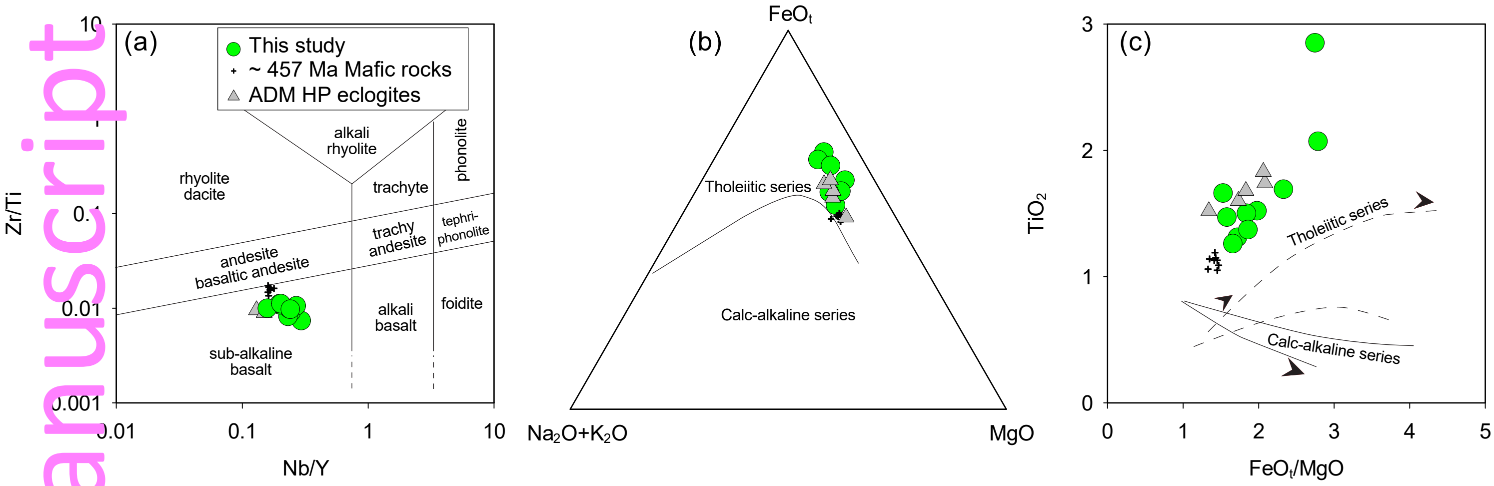
(a)
This study
~ 457 Ma Mafic rocks
ADM HP eclogites
Zr/Ti
Nb/Y
10
0.1
0.01
0.001
0.01
1
rhyolite dacite
alkali rhyolite
phonolite
trachyte
trachy andesite
tephri-phonolite
andesite basaltic andesite
alkali basalt
foidite
sub-alkaline basalt
(b)
FeOt
Na2O+K2O
MgO
Tholeiitic series
Calc-alkaline series
(c)
TiO2
FeOt/MgO
0
1
2
3
4
5
Tholeiitic series
Calc-alkaline series

Figure 6

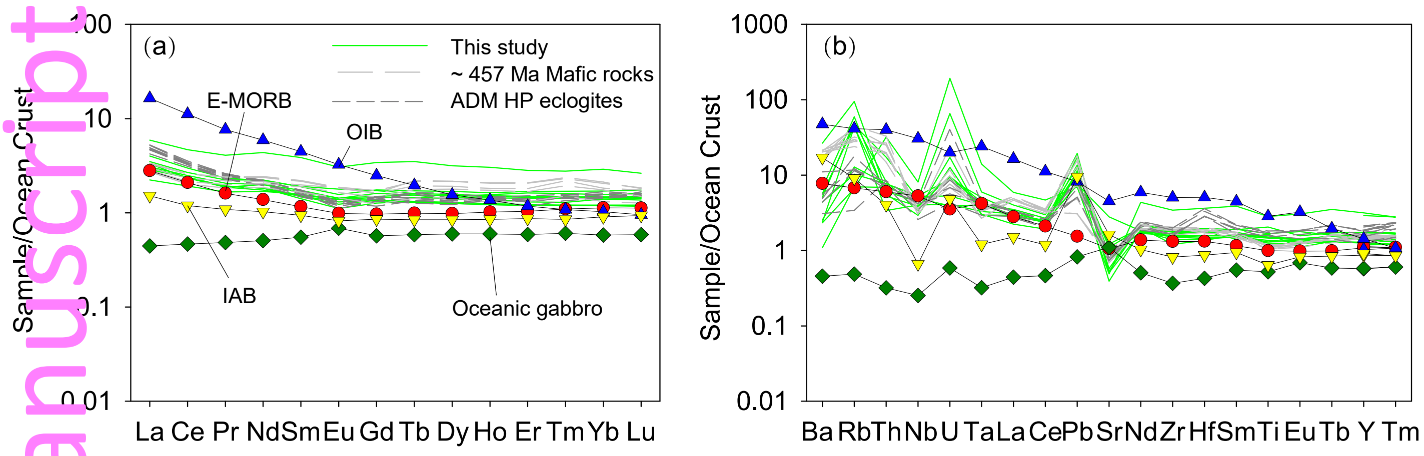

(a)
This study
~ 457 Ma Mafic rocks
ADM HP eclogites
E-MORB
OIB
IAB
Oceanic gabbro
Sample/Ocean Crust
100
10
1
0.1
0.01
La Ce Pr Nd Sm Eu Gd Tb Dy Ho Er Tm Yb Lu
(b)
Sample/Ocean Crust
1000
100
10
1
0.1
0.01
Ba Rb Th Nb U Ta La Ce Pb Sr Nd Zr Hf Sm Ti Eu Tb Y Tm

Figure 7

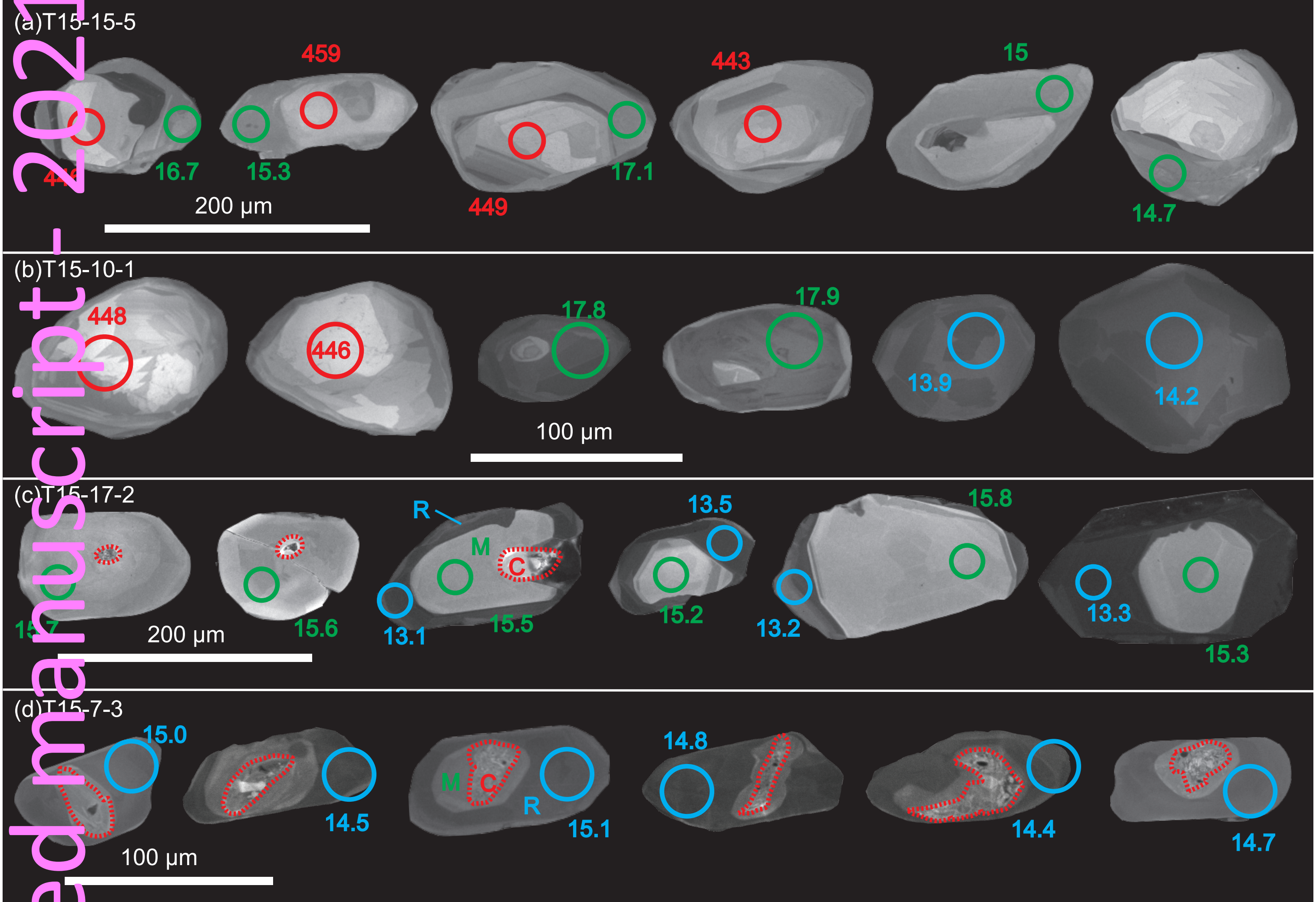

(a)T15-15-5
459
443
15
16.7
15.3
17.1
449
14.7
200 µm
(b)T15-10-1
448
446
17.8
17.9
13.9
14.2
100 µm
(c)T15-17-2
R
M
C
13.5
15.8
15.6
13.1
15.5
15.2
13.2
13.3
15.3
200 µm
(d)T15-7-3
15.0
14.5
M
C
R
15.1
14.8
14.4
14.7
100 µm

Figure 8

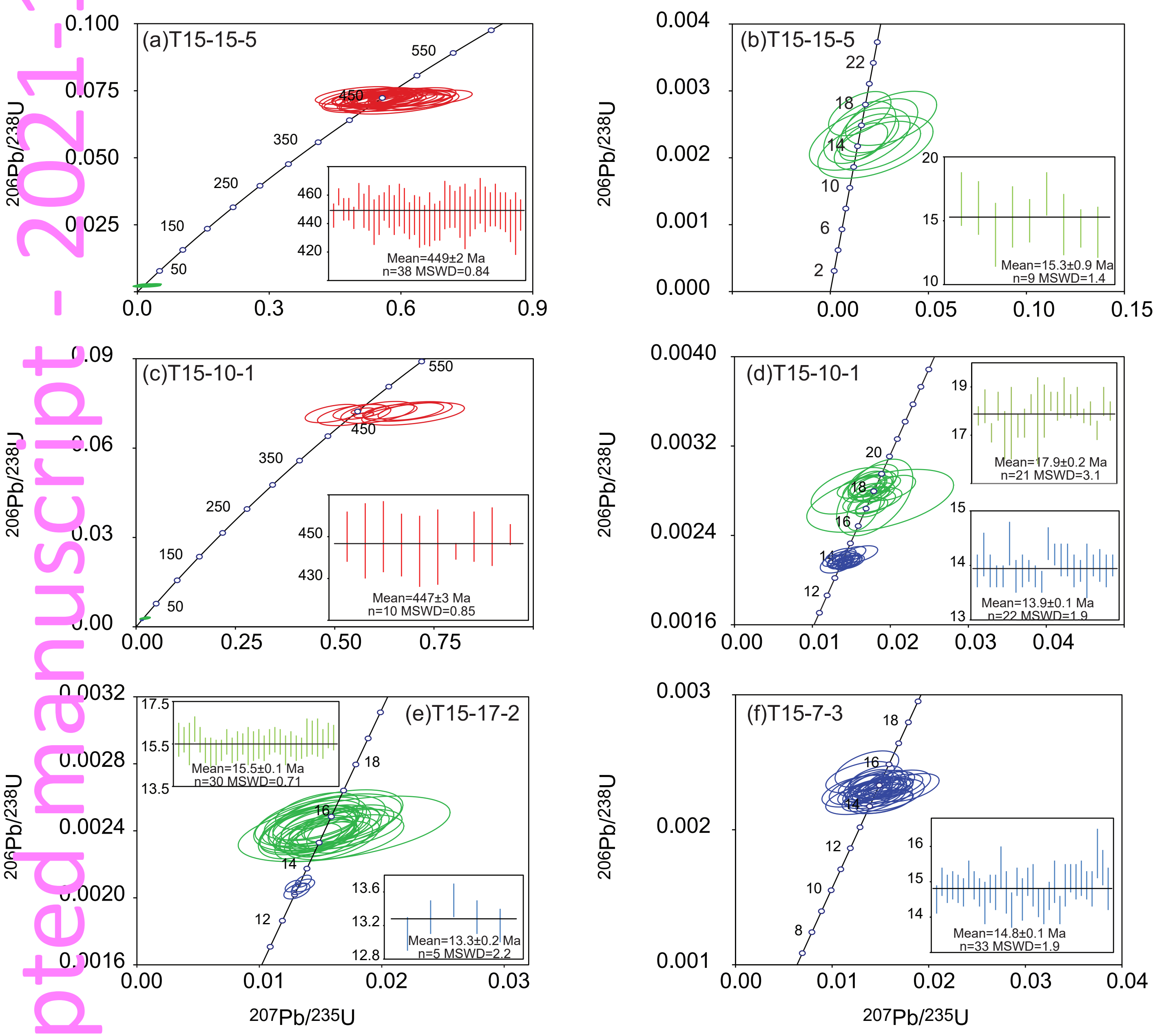

(a)T15-15-5
Mean=449±2 Ma
n=38 MSWD=0.84
(b)T15-15-5
Mean=15.3±0.9 Ma
n=9 MSWD=1.4
(c)T15-10-1
Mean=447±3 Ma
n=10 MSWD=0.85
(d)T15-10-1
Mean=17.9±0.2 Ma
n=21 MSWD=3.1
Mean=13.9±0.1 Ma
n=22 MSWD=1.9
(e)T15-17-2
Mean=15.5±0.1 Ma
n=30 MSWD=0.71
Mean=13.3±0.2 Ma
n=5 MSWD=2.2
(f)T15-7-3
Mean=14.8±0.1 Ma
n=33 MSWD=1.9
206Pb/238U
207Pb/235U

Figure 9

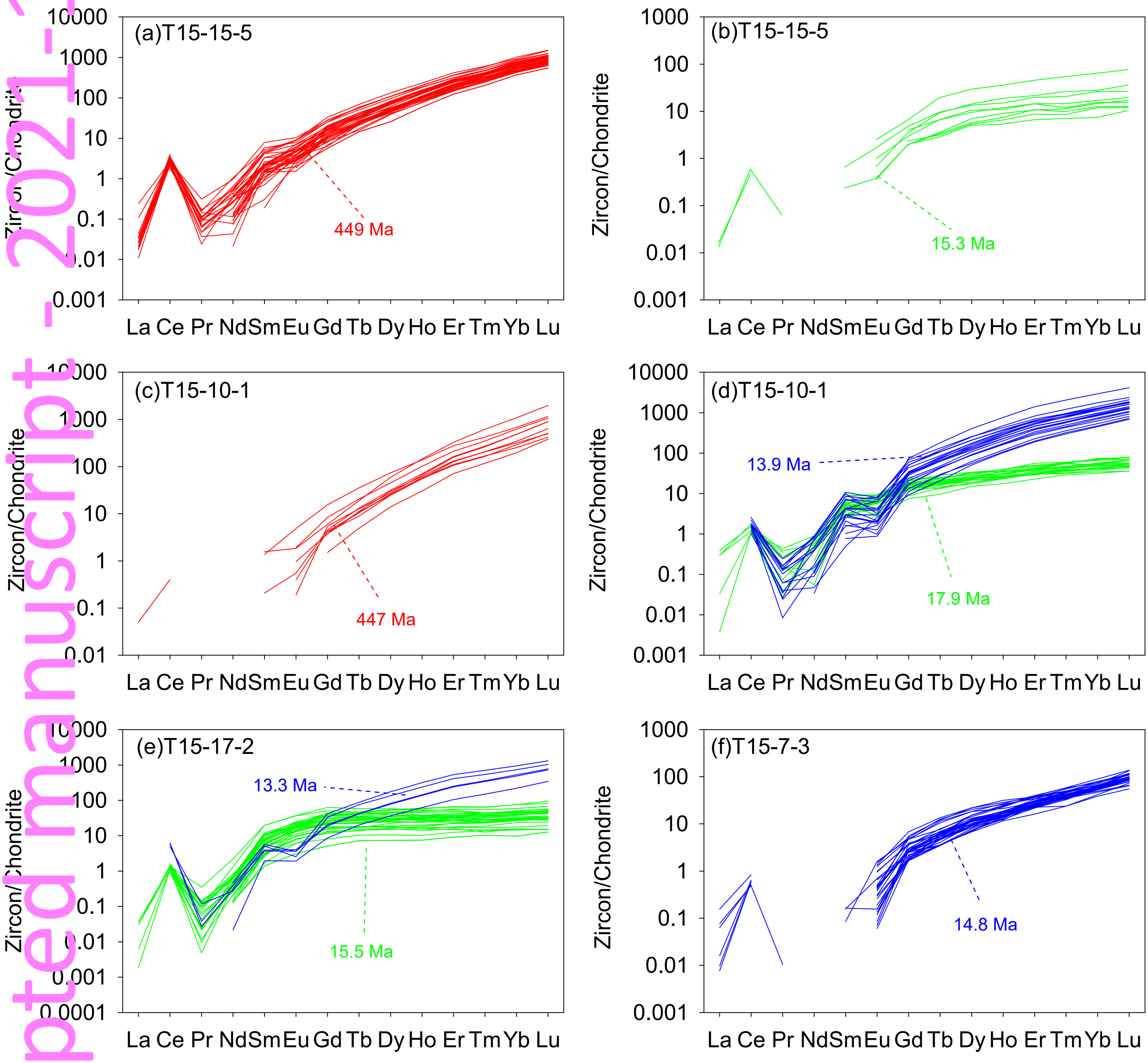
(a)T15-15-5
449 Ma
(b)T15-15-5
15.3 Ma
(c)T15-10-1
447 Ma
(d)T15-10-1
13.9 Ma
17.9 Ma
(e)T15-17-2
13.3 Ma
15.5 Ma
(f)T15-7-3
14.8 Ma
Zircon/Chondrite
0.0001
0.001
0.01
0.1
1
10
100
1000
10000
La Ce Pr Nd Sm Eu Gd Tb Dy Ho Er Tm Yb Lu

Figure 10

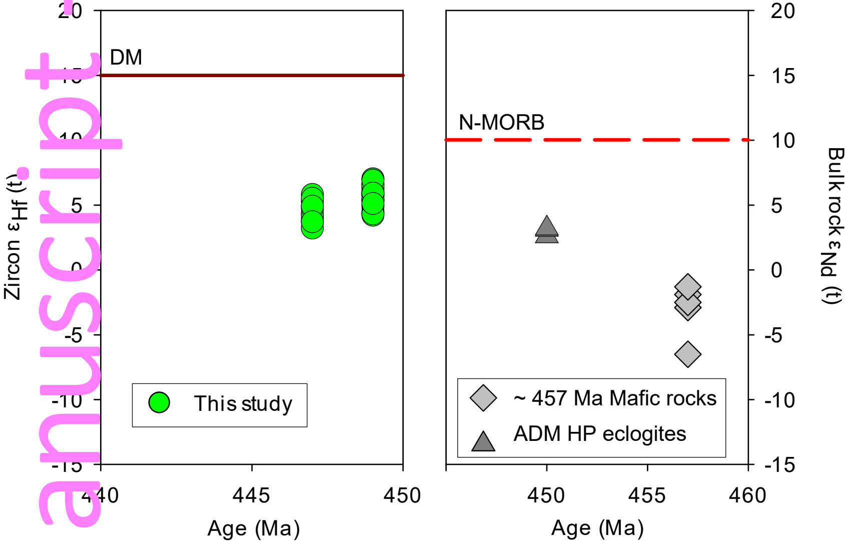

DM
N-MORB
Zircon εHf (t)
Bulk rock εNd (t)
This study
~ 457 Ma Mafic rocks
ADM HP eclogites
Age (Ma)
Age (Ma)
20
15
10
5
0
-5
-10
-15
440
445
450
450
455
460

Figure 11

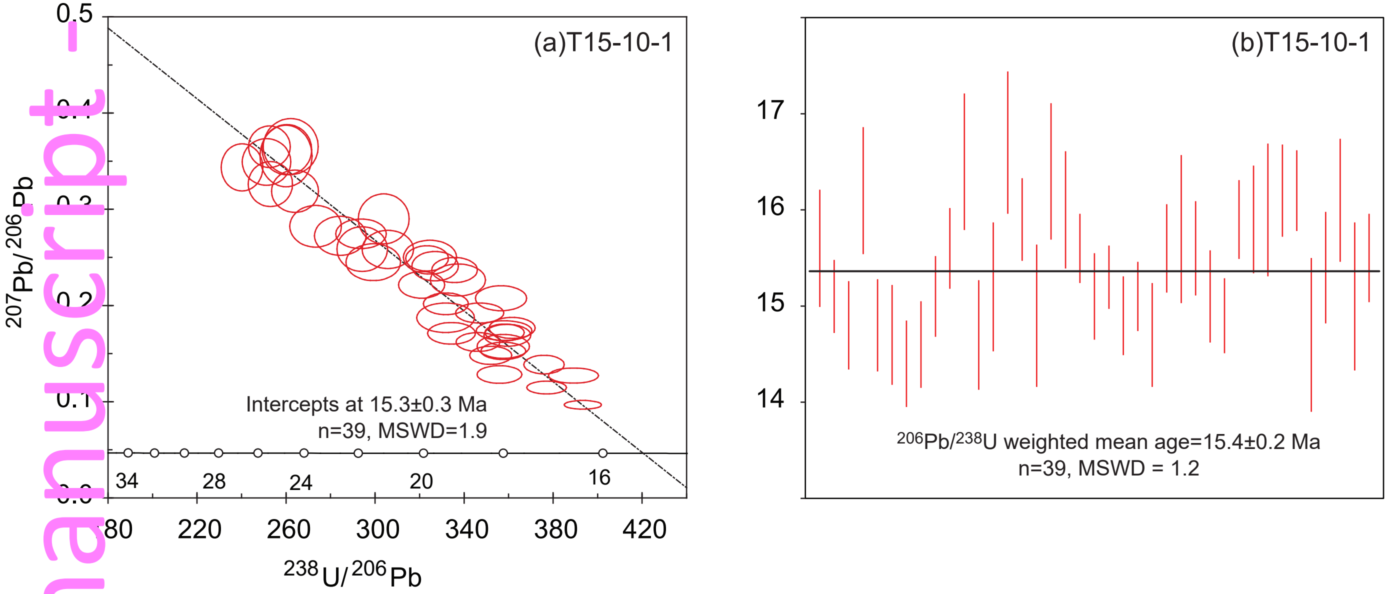
(a)T15-10-1
0.5
0.4
0.3
0.2
0.1
0.0
$^{207}Pb/^{206}Pb$
Intercepts at 15.3±0.3 Ma
n=39, MSWD=1.9
34
28
24
20
16
180
220
260
300
340
380
420
$^{238}U/^{206}Pb$
(b)T15-10-1
17
16
15
14
$^{206}Pb/^{238}U$ weighted mean age=15.4±0.2 Ma
n=39, MSWD = 1.2

Figure 12

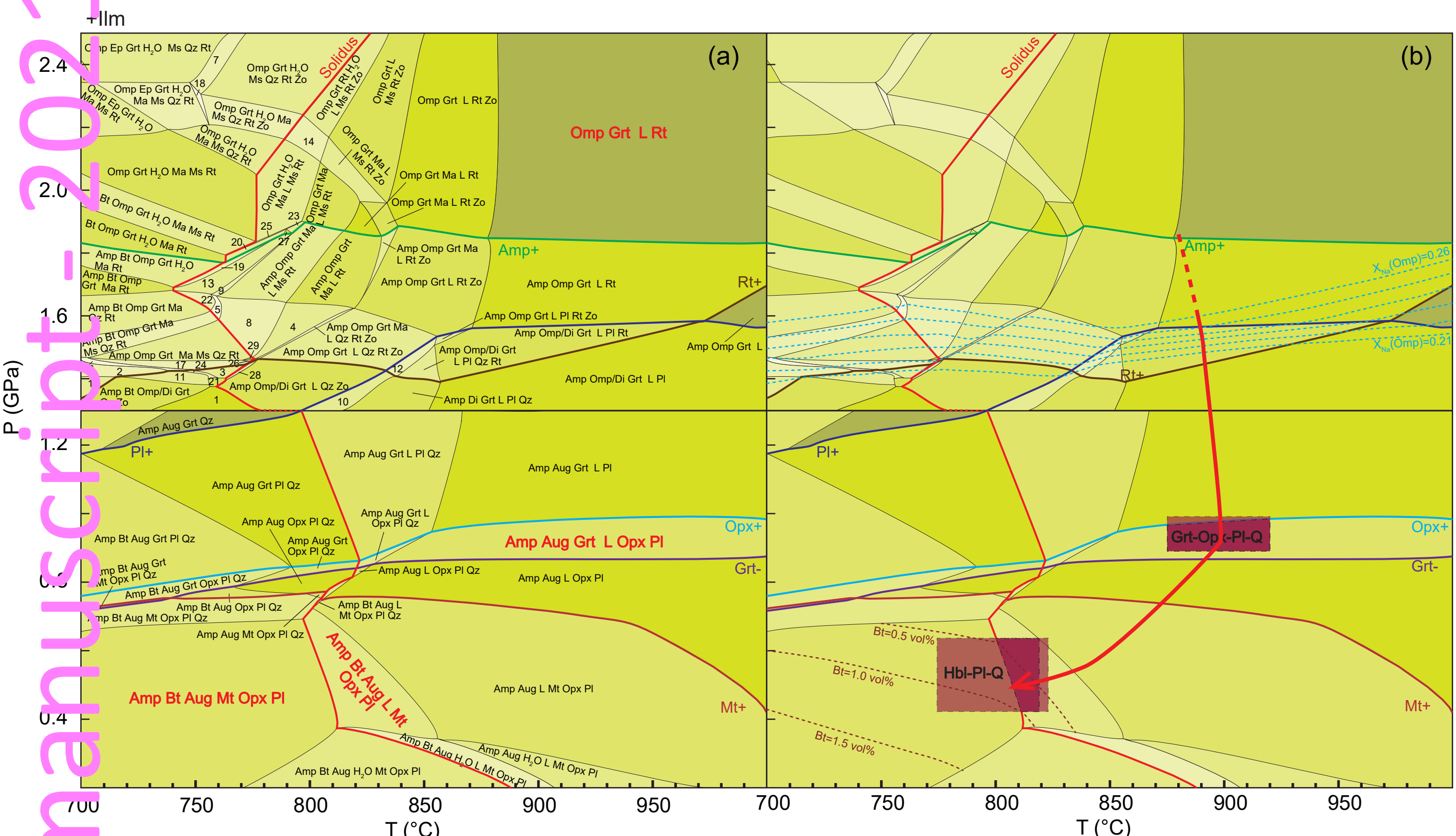

1 Amp Di Grt Qz Zo
2 Amp Bt Omp Grt Ma Qz Rt Zo
3 Amp Omp Grt Ma Ms Qz Zo
4 Amp Omp Grt Ma L Qz Rt
5 Amp Bt Omp Grt Ma L Ms Qz Rt
6 Omp Ep Grt H_2O Ms Rt
7 Omp Ep Grt H_2O Ms Qz Rt Zo
8 Amp Omp Grt Ma L Ms Qz Rt
9 Amp Bt Omp Grt Ma L Ms Rt
10 Amp Omp/Di Grt L Pl Qz Zo
11 Amp Bt Omp Grt Ma Qz Zo
12 Amp Omp Grt L Pl Qz Rt Zo
13 Amp Bt Omp Grt Ma L Rt
14 Omp Grt H_2O Ma L Ms Rt Zo
15 Amp Bt Omp Grt Qz Rt Zo
16 Amp Bt Omp Grt Ma Ms Qz Rt Zo
17 Amp Omp Grt Ma Ms Qz Rt Zo
18 Omp Ep Grt H_2O Ma Ms Qz Rt Zo
19 Amp Bt Omp Grt H_2O Ma L Rt
20 Bt Omp Grt H_2O Ma L Rt
21 Amp Omp Grt Ma Qz Zo
22 Amp Bt Omp Grt Ma L Qz Rt
23 Bt Omp Grt Ma L Ms Rt
24 Amp Bt Omp Grt Ma Ms Qz Zo
25 Bt Omp Grt H_2O Ma L Ms Rt
26 Amp Omp Grt Ma Qz Rt Zo
27 Bt Omp Grt Ma L Rt
28 Amp Omp Grt Ma L Ms Qz Zo
29 Amp Omp Grt Ma Qz Rt

Figure 13

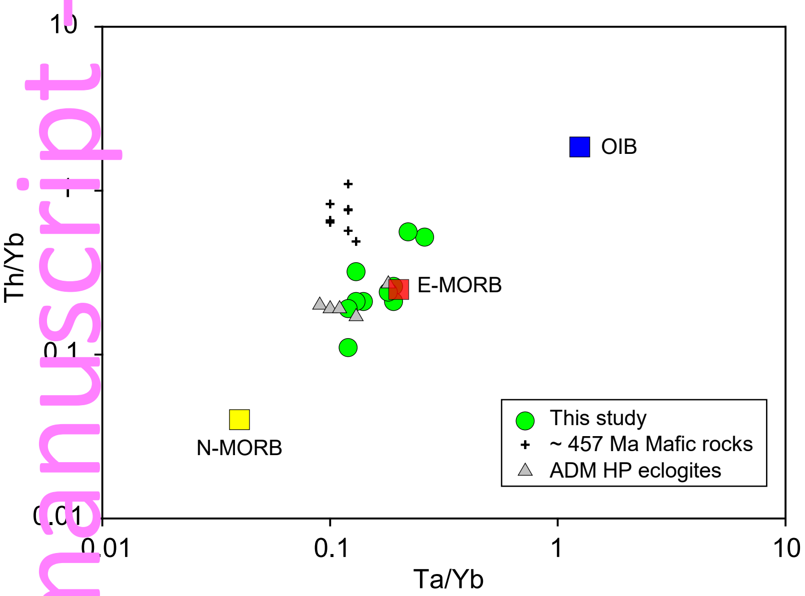
10
0.1
0.01
0.01
0.1
1
10
Th/Yb
Ta/Yb
OIB
E-MORB
N-MORB
This study
~ 457 Ma Mafic rocks
ADM HP eclogites

Figure 14

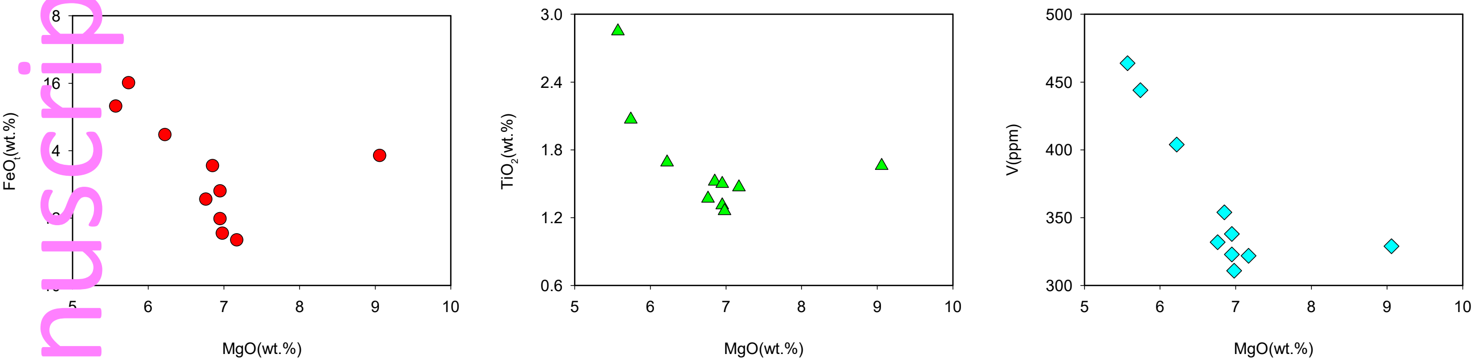

Figure 15

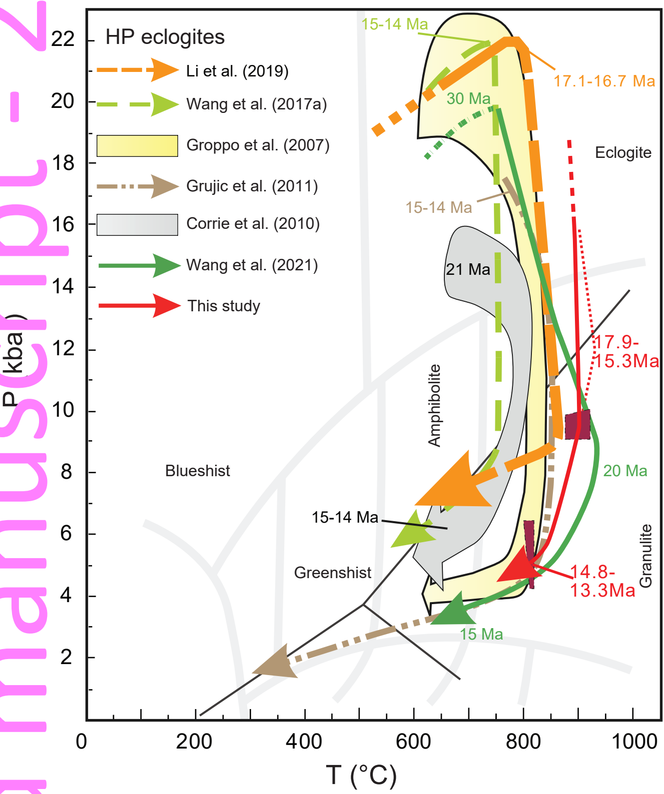
HP eclogites
Li et al. (2019)
Wang et al. (2017a)
Groppo et al. (2007)
Grujic et al. (2011)
Corrie et al. (2010)
Wang et al. (2021)
This study
15-14 Ma
17.1-16.7 Ma
30 Ma
Eclogite
15-14 Ma
21 Ma
17.9-
15.3Ma
Amphibolite
20 Ma
Blueshist
15-14 Ma
Greenshist
14.8-
13.3Ma
Granulite
15 Ma
22
20
18
16
14
12
10
8
6
4
2
P (kbar)
0
200
400
600
800
1000
T (°C)

Figure 16